Archean Pb isotope variability tracks crust-mantle fractionation, granite production, and ore deposit formation

Andreas Zametzer [a],[*], Christopher L. Kirkland [a], Milo Barham [a], R. Hugh Smithies [b],[a], David L. Huston [c], David C. Champion [c]

[a] *Timescales of Mineral Systems Group, School of Earth and Planetary Sciences (EPS), Curtin University, GPO Box U1987, Perth, WA 6845, Australia*
[b] *Geological Survey of Western Australia, Department of Mines, Industry Regulation and Safety, Mineral House, 100 Plain Street, East Perth, WA 6004, Australia*
[c] *Geoscience Australia, GPO Box 378, Canberra, ACT 2601, Australia*

ARTICLE INFO

ABSTRACT

Various geological processes that affect Earth's crust may be encoded into isotopic tracers preserved in rocks and minerals. The enhanced sensitivity of U, Th, and Pb to crustal fractionation processes allows Pb isotopes to complement information from the Nd and Hf isotope systems. However, melt fractionation, crustal contamination and recycling, hydrothermal fluid flow and fluid-rock interaction, and other processes in the continental crust can lead to mixing of Pb isotopic signatures. Here, we report new Pb isotopic data from granite-K-feldspar and integrate these data with published Pb isotope ratios from granite K-feldspar and Pb-rich ores across the Yilgarn Craton in Western Australia. The aim of this study is to explore how the variability of Pb isotope ratios and derivative parameters can be used to gain information on specific geological processes occurring throughout the crustal column. We develop a model that subdivides different sampling media into chemical process groups and links their initial Pb signatures to Pb source regions and fractionation processes at various locations within the crust and upper mantle. Equilibration of Pb signatures with a primary mantle source reservoir (in part represented by volcanic-hosted massive sulfides) is contrasted with granite formation in the mid to lower crust (granite K-feldspar), and mineralization of ore deposits in the mid to upper crust (Pb-rich ores). Spatial trends similar to those in Nd and Hf isotopic data are recorded by Pb isotopic derivative parameters (μ = source $^{238}U/^{204}Pb$, ω = $^{232}Th/^{204}Pb$, and Δt - the difference between true sample age and Pb model age) calculated for komatiite-hosted Ni sulfide ores, granite K-feldspar, and volcanic-hosted massive sulfide (VHMS) ores. The significance of subtle differences in absolute values of derivative parameters is supported by the diversity of Pb isotope ratios, Pb model ages, and Δt as tracked by a statistical metric, quantifying the variability of Pb sources involved in the formation of different chemical process groups. Generally greater variety in an older terrane (Youanmi) documents more ancient and recycled continental crust as compared with more homogeneous Pb isotopic signatures in a younger terrane (Eastern Goldfields Superterrane). The Pb signatures are interpreted, in part, to relate to the timing of source fractionation in the upper mantle with a legacy of this source signal preserved through various depths in the lithospheric section. The least radiogenic VHMS ore samples appear to provide a good approximation of mantle Pb signatures, indicated for example by a deficit in ^{206}Pb and ^{208}Pb relative to the other process groups. A significant heterogeneity recorded in Pb isotopic data from Pb-rich gold ores is explained by the interplay of hydrothermal fluids with diverse sources leading to the mineralization of gold deposits (e.g., leaching of Pb from surrounding rocks or fluid mixing). Such gold ore Pb signatures are distinct from other process groups, which together track sources less heterogeneous in age and/or U and Th.

1. Introduction

The generation, evolution, and recycling of Earth's continental crust results from a complex interplay of a plethora of geological processes (Taylor and McLennan, 1985; Albarède, 1998; Hawkesworth and Kemp, 2006a, 2006b; Bolhar et al., 2007; Hawkesworth et al., 2010, 2016; Kamber, 2015; Korenaga, 2018). A planetary-scale driver of the processes that ultimately resulted in the continental crust is heat, in part

produced from the decay of radioactive parent isotopes (e.g., Campbell and Hill, 1988; Cooper et al., 2006; Huang et al., 2013a). The bulk of this thermal energy originates from the lower mantle and flows towards other compositional reservoirs in the chemically and physically stratified Earth: the 'depleted' upper mantle, the lower continental crust, and the upper continental crust (Taylor and McLennan, 1985; McDonough and Sun, 1995; Paul et al., 2002).

Elemental fluxes between these different reservoirs can be tracked through time using different isotope systems and sampling media to target specific geological processes. Over the last twenty years, Nd and Hf isotopes have become frequently applied tools to track the relative significance of juvenile mantle input and crustal reworking in magmas (e.g., Champion, 2013; Mole et al., 2014, 2019; Bolhar et al., 2017; Gardiner et al., 2017; Agangi et al., 2018). Model ages of the Nd and Hf systems are interpreted as the time when a particular element was in isotopic equilibrium with its source reservoir (typically the upper mantle), and thus approximate an average age of source component extraction from the mantle (e.g., DePaolo, 1988; Kinny and Maas, 2003; Hawkesworth and Kemp, 2006b). Hence, they provide a mechanism to constrain the broad timing of crust-mantle fractionation at deeper crustal levels.

The isotopic composition of Pb on the other hand is much more sensitive to crustal fractionation processes than Nd and Hf signatures due to the enhanced lithophile nature of U, Th, and Pb. Incompatible elements like U and Th have high valence and ionic charge and large ionic radii, which leads to misfits in interstitial sites in most mantle minerals (e.g., Hofmann, 1997). Thus, U and Th both fractionate into the crust during partial melting of the mantle and are enriched in the continental crust by a factor of >20, while Pb shows lithophile tendencies and a certain enrichment in the continental crust as well (Taylor and McLennan, 1985). The Pb isotope system is therefore better able than Nd or Hf isotopes to image chemical and physical processes taking place at mid to upper crustal levels, including melting, fractionation, magma mixing, crustal contamination, and mineralization (e.g., Blaxland et al., 1979; Moorbath and Taylor, 1981; Browning et al., 1987; Wareham et al., 1998; Miller et al., 2000; Huston et al., 2005, 2014; Halla, 2014, 2018b; Champion and Huston, 2016; Arcuri and Dickin, 2018). Consequently, Pb isotopes can contribute to unravelling the process history archived in Archean terranes and distinguishing between mantle- and crust-related signatures (Krishna Sinha and Tilton, 1973; Davis et al., 1996; Gruau et al., 1996; Isnard and Gariépy, 2004; Ram Mohan et al., 2013; Kamber, 2015; Petrus et al., 2016). Historically, Pb isotopes have been fundamental in establishing geochemical knowledge on the formation and evolution of early continental crust (e.g, Kanasewich and Farquhar, 1965; Moorbath et al., 1969; Krishna Sinha and Tilton, 1973; Oversby, 1975, 1976, 1978; Gancarz and Wasserburg, 1977). However, Pb isotopes have arguably lost some popularity in recent decades owing to laborious analytical procedures traditionally required in their analysis. Laser ablation sampling of suitable Pb-enriched but U- and Th-poor minerals may offer a mechanism to rapidly gain insight into regional Pb isotopic patterns.

Here, we measure Pb isotopic data from eight granite K-feldspar samples from the Yilgarn Craton in Western Australia, using laser ablation, and complement this with a compilation of published measurements from granite K-feldspar and Pb-rich ores. Derivative parameters (μ = reservoir $^{238}U/^{204}Pb$; ω = $^{232}Th/^{204}Pb$; κ = $^{232}Th/^{238}U$; Pb model ages; Δt = the difference between true sample age and Pb model age) of the Pb isotope system are calculated after choosing regionally appropriate Pb evolution models. The aim of this contribution is a synthesis of Pb isotopes across the Yilgarn Craton. By combining Pb isotopic data (from granite K-feldspar and Pb-rich ore minerals like galena from volcanic-hosted massive sulfide (VHMS), gold, and komatiite-hosted Ni sulfide deposits) with Nd (granite whole rock) and Hf (zircon) we shed light on the role of geological processes responsible for the transfer of U, Th, and Pb within the continental crust. We identify trends laterally and vertically within the crustal column, and hence investigate how deep and shallow fractionation processes may operate and result in process-dependent Pb isotope heterogeneity that can be statistically tracked.

2. Study area – the Yilgarn Craton

The Yilgarn Craton in Western Australia is an ideal study area to investigate crust generation and evolution, and the structure of the early lithosphere as: 1) It is one of the largest preserved blocks of Precambrian lithosphere on Earth (e.g., Gee, 1979). 2) The mostly Meso- to Neoarchean rocks of the Yilgarn Craton represent an archive of an important episode of voluminous crustal growth (~2800–2500 Ma; e.g., Condie, 2000; Condie and Alster, 2010; Hawkesworth et al., 2010, 2017; Condie and Kröner, 2013; Kamber, 2015; Cawood et al., 2018). 3) Economic interest in the Yilgarn Craton has led to a detailed picture of its regional geology. The Yilgarn Craton is economically significant due to its endowment with gold and other metals (e.g., Blewett et al., 2010b; McCuaig et al., 2010) which has resulted in numerous isotopic maps (isoscapes) and large-scale seismic transects through the craton. Whole rock Nd isoscapes include those by Champion and Sheraton (1997), Cassidy and Champion (2004), Champion (2013), Mole et al. (2013), Lu et al. (2021a), and Osei et al. (2021). Zircon Hf isoscapes include those by Wyche et al. (2012), Mole et al. (2014, 2019), Lu et al. (2021b), and Osei et al. (2021). All these studies, combined with detailed field investigations, have helped to unravel the structural geology and metallogenesis of the craton. Many magmatic components (and especially the widespread granites) have been accurately dated via U-Pb zircon geochronology (e.g., Pidgeon and Wilde, 1990; Nelson, 1997a, 1997b, 1998, 1999; Qiu and McNaughton, 1999; Fletcher et al., 2001; Dunphy et al., 2003). These factors make the Yilgarn Craton a comparatively well understood Archean crustal section.

The Yilgarn Craton is defined by a granite-greenstone stratigraphy with an approximate overall proportion of 70 % granites and gneisses and 30 % greenstones (Wyche and Wyche, 2017; Fig. 1a). The craton has been divided into the western Yilgarn Craton, comprising the Youanmi Terrane, as well as the Narryer and the South West terranes, and the Eastern Goldfields Superterrane (EGST; Cassidy et al., 2006; Quentin de Gromard et al., 2021; Fig. 1). The Youanmi Terrane consists of the Murchison Domain in the west and the Southern Cross Domain in the east (Fig. 1). The EGST is further subdivided into the Kalgoorlie, Kurnalpi, Burtville, and Yamarna terranes from west to east (Cassidy et al., 2006; Pawley et al., 2012; Fig. 1). The Ida Fault, a more than 750 km long, north-south extending, crustal-scale, eastward dipping fault, separates the western Yilgarn Craton, and more specifically the Youanmi Terrane, from the EGST (Fig. 1b). This listric normal fault was active during the late-stage Neoarchean geodynamic evolution of the Yilgarn Craton between ~2700 Ma and 2600 Ma (Swager et al., 1997; Drummond et al., 2000; Goleby et al., 2006; Blewett et al., 2010b; Wyche et al., 2013; Fig. 1b). The Ida Fault is generally well resolved on seismic images (Wyche et al., 2013) and on Sm-Nd (Champion, 2013; Fig. 1a) and Lu-Hf isotopic maps (Mole et al., 2019), as well as by differences in U-Pb zircon crystallization ages (Nelson, 1997a, 1997b, 1998, 1999; Fletcher et al., 2001; Dunphy et al., 2003; Van Kranendonk et al., 2013; Mole et al., 2019). The average thickness of the crust in the Yilgarn Craton is ~35 km with thicker sections of up to 48 km in the eastern EGST (Swager et al., 1997; Blewett et al., 2010b).

Between the Forrestania, Kambalda, and Norseman greenstone belts at the southern margin of the Yilgarn Craton (Fig. 1) a large-scale isotopic anomaly was identified in Pb isotopes (Oversby, 1975, 1978), Nd, and U-Pb zircon (Compston et al., 1986; Campbell and Hill, 1988), and in Hf isotopic data sets (Mole et al., 2014, 2019). This anomaly is usually interpreted as indicative of ancient protocrust (Kamber et al., 2003, 2005). A case has been made for plume-driven continental rifting initiated by mafic and ultramafic magmatism at ~2900 Ma in the southern Youanmi Terrane and at ~2700 Ma in the EGST (Barnes et al., 2012; Mole et al., 2014). Large-scale extension in a late stage of the
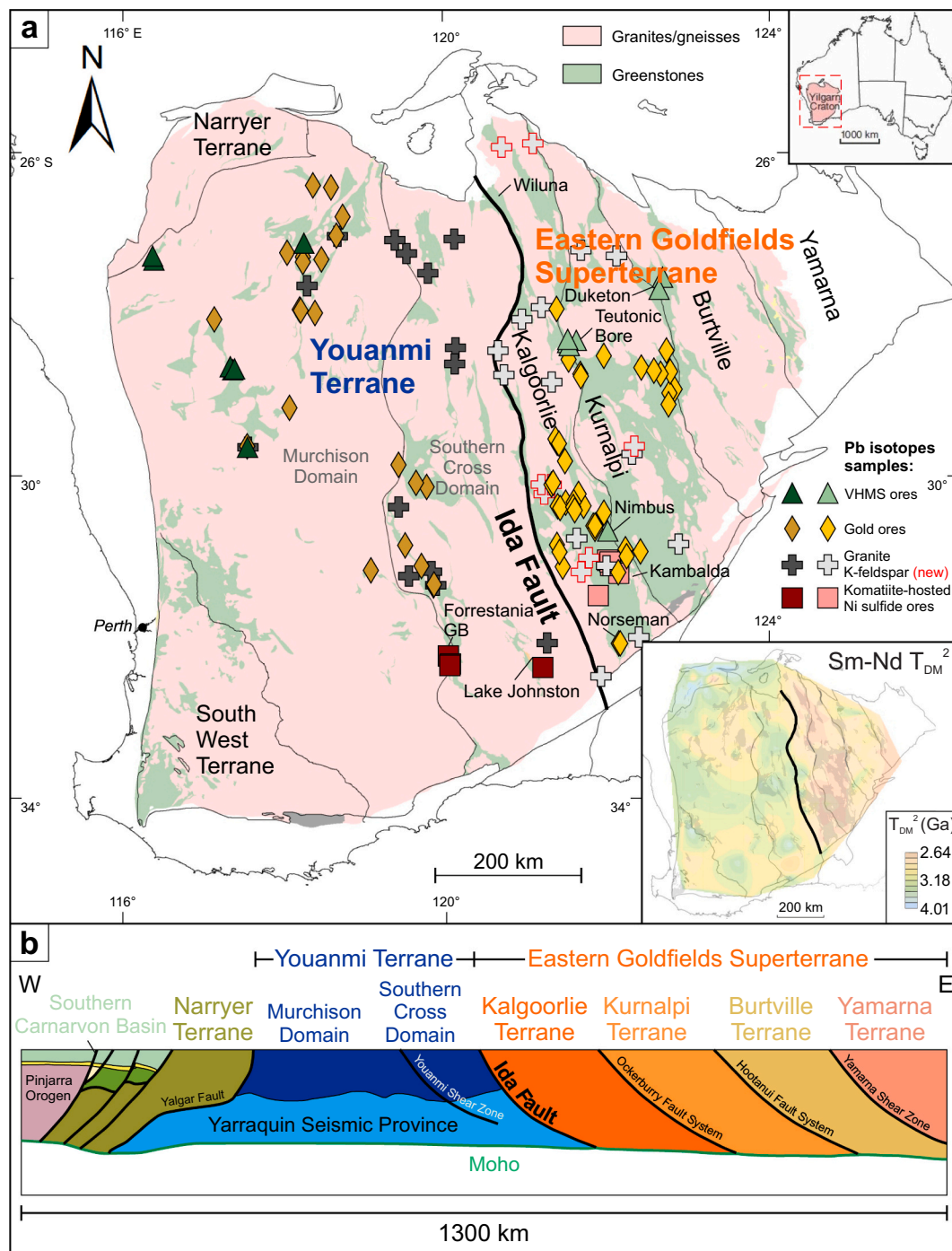
Fig. 1. a) Overview map of the Yilgarn Craton with terrane boundaries (following Cassidy et al., 2006, and Quentin de Gromard et al., 2021), simplified granites vs. greenstone geology, and the locations of all samples used for Pb isotope ratio analysis. Modified after Zametzer et al. (2022). The Pb isotopic data from granite K-feldspar samples with red outlines are newly published in this study. Inset Nd two-stage model map modified after Cassidy and Champion (2004), Champion (2013), and Wyche et al. (2019). b) Generalized cross-section of the Yilgarn Craton and terrane-bounding faults and shear zones based upon cross-sections and seismic profiles in Wyche et al. (2013). The east-dipping Ida Fault is the major crustal-scale boundary between the Youanmi Terrane and the Eastern Goldfields Superterrane. (For interpretation of the references to colour in this figure legend, the reader is referred to the web version of this article.)

geodynamic evolution of the Yilgarn Craton is documented (Czarnota et al., 2010; Mole et al., 2012; Calvert and Doublier, 2018). The time interval between ~2700 Ma and 2600 Ma was characterized by a craton-wide granite bloom followed by widespread cratonization (Kent et al., 1996; Cassidy et al., 2002; Czarnota et al., 2010; Mole et al., 2012, 2019; Rowe et al., 2022).

3. Principles and applications of the Pb isotope system

3.1. Pb growth systematics and Pb isotope derivative parameters

Evaluating the source of crustal rocks using Pb isotopes requires the direct measurement or calculation of the initial Pb isotope composition (common Pb), which is defined as any Pb that is incorporated into a crystal or rock at the time of formation (t_2). Uranogenic Pb results from

the decay of ^{238}U and ^{235}U to ^{206}Pb and ^{207}Pb, respectively, and thorogenic Pb from the decay of ^{232}Th to ^{208}Pb in the source reservoir. The common Pb composition of a given rock contains information on the U–Th–Pb decay history and the U/Pb and Th/Pb ratio of the source material. Crystallization or mineralization at t_2 are typical processes that isolate the Pb isotope signal of geological materials from their source reservoir.

Ideal sampling media for Pb isotopes are galena, Pb sulfosalts, Pb selenides, and Pb tellurides, which incorporate Pb but essentially no U and Th during crystallization, and therefore detach the Pb isotope composition from the decay of parent U or Th isotopes (Stacey and Kramers, 1975; Fletcher and Farquhar, 1982). Sulfides such as pyrite and K-feldspar mostly have U/Pb and Th/Pb ratios close to zero and can provide a reliable approximation of source composition, as they are minimally affected by radiogenic ingrowth (e.g., Doe, 1967; Oversby, 1975, 1978; Gariépy and Allègre, 1985; Kramers and Tolstikhin, 1997; Halla, 2005). Nevertheless, Zametzer et al. (2022) demonstrated mathematically that even a relatively small amount of U or Th in an Archean mineral, for instance through micro-inclusions or secondary minerals in cracks within feldspars (e.g., Housh and Bowring, 1991; McNamara et al., 2017), can substantially affect Pb isotopic signatures. Ludwig and Silver (1977) highlighted that radiogenic Pb may be deposited in K-feldspar through post-magmatic fluids and not bound in the feldspar lattice. Such unsupported radiogenic Pb may be able to be removed by acid-leaching prior to isotopic analysis (Ludwig and Silver, 1977).

The isotopes ^{206}Pb, ^{207}Pb, and ^{208}Pb are usually measured and displayed relative to the primordial and non-radiogenic ^{204}Pb. The most important derivative parameters of the Pb isotope system are μ (= ^{238}U/^{204}Pb ratio in the reservoir) and ω (= ^{232}Th/^{204}Pb in the reservoir), denoting the abundances of U and Th relative to ^{204}Pb, as well as κ (= ^{232}Th/^{238}U in the reservoir), and Pb model ages.

The evolution of ^{206}Pb/^{204}Pb, ^{207}Pb/^{204}Pb, and ^{208}Pb/^{204}Pb isotopic ratios in a source system, beginning at a start date t_1 is described by the following general equations (Houtermans, 1946):

$$\left(\frac{^{206}Pb}{^{204}Pb}\right)_{t_2} = \left(\frac{^{206}Pb}{^{204}Pb}\right)_{t_1} + \mu \times \left(e^{\lambda_x \times t_1} - e^{\lambda_x \times t_2}\right) \tag{1}$$

$$\left(\frac{^{207}Pb}{^{204}Pb}\right)_{t_2} = \left(\frac{^{207}Pb}{^{204}Pb}\right)_{t_1} + \left(\frac{\mu}{\frac{^{238}U}{^{235}U}}\right) \times \left(e^{\lambda_y \times t_1} - e^{\lambda_y \times t_2}\right) \tag{2}$$

$$\left(\frac{^{208}Pb}{^{204}Pb}\right)_{t_2} = \left(\frac{^{208}Pb}{^{204}Pb}\right)_{t_1} + \omega \times \left(e^{\lambda_z \times t_1} - e^{\lambda_z \times t_2}\right) \tag{3}$$

Equations Eqs. (1) to (3) make predictions about expected ^{206}Pb/^{204}Pb, ^{207}Pb/^{204}Pb, and ^{208}Pb/^{204}Pb ratios of the investigated material at the time t_2 of decoupling from the source. Decay constants after Jaffey et al. (1971) for the uranium isotopes (^{238}U: λ_x = 1.55125*10^{-10} ± 0.00166*10^{-10} yr^{-1}; ^{235}U: λ_y = 9.8485*10^{-10} ± 0.0135*10^{-10} yr^{-1}) and after Steiger and Jäger (1977) for the thorium isotope (^{232}Th: λ_z = 4.9475*10^{-11} ± 0.0495*10^{-11} yr^{-1}) are applied in all calculations in this paper.

A present-day ^{238}U/^{235}U ratio of 137.88 after Steiger and Jäger (1977) has been used in many published Pb evolution models (e.g., Stacey and Kramers, 1975), before workers tried to refine this parameter (see Goldmann et al., 2015, and Andersen et al., 2017, for recent reviews). Technical advances in mass spectrometry have led to newly defined ^{238}U/^{235}U ratios, amongst which 137.818 published by Hiess et al. (2012) and based on zircon analyses is frequently applied. This value has been validated by Livermore et al. (2018) and is generally representative of the continental crust, even though it might induce a certain bias for felsic lithologies. Maltese and Mezger (2020) chose a very similar value (137.82) as proxy for the Bulk Silicate Earth. Since various sampling media that formed in or are part of the continental crust are examined in this paper, we consistently use a ^{238}U/^{235}U value of 137.818 in all calculations (Hiess et al., 2012).

3.2. Pb evolution models

The aim of Pb evolution models is to approximate Pb growth (Eq.1, Eq.2, and Eq.3) in geochemical reservoirs (e.g., upper mantle, lower continental crust etc.). In order to define a Pb evolution model, initial Pb ratios at a start date t_1 have to be quantified (Oversby, 1974). These initial Pb compositions can be measured isotopic compositions of the most primitive sample materials available (termed primordial Pb; Blichert-Toft et al., 2010), e.g., meteorites like the Canyon Diablo troilite (Oversby, 1970). Alternatively, initial Pb ratios which are linked to a well-constrained geological event at t_1 can be deduced if this event is thought to have influenced the U–Th–Pb scheme on the scale of the investigated reservoir (e.g., Stacey and Kramers, 1975; Kramers and Tolstikhin, 1997; Kamber and Collerson, 1999; Maltese and Mezger, 2020).

Models also require the quantification of μ, ω, and κ which would typically happen by aligning best-fit curves through data from samples that are representative of the modelled reservoir (often galena sample sets; e.g., Stanton and Russell, 1959; Stacey et al., 1969; Oversby, 1974; Stacey and Kramers, 1975). A change in the reservoir μ or κ value will lead to the introduction of a second step of Pb evolution in a model. Numerous single-stage (Holmes, 1946; Houtermans, 1946; Stanton and Russell, 1959; Stacey et al., 1969; Maltese and Mezger, 2020), two-stage (Stacey and Kramers, 1975; Kamber and Collerson, 1999), or multi-stage (Doe and Zartman, 1979; Zartman and Doe, 1981; Zartman and Haines, 1988; Kramers and Tolstikhin, 1997; Bolhar et al., 2007) Pb evolution models have been defined. Cumming and Richards (1975) and Gancarz and Wasserburg (1977) developed models accounting for open-system behavior of Pb where μ and ω change continuously. However, the linear change of μ and ω through time in Cumming and Richards' (1975) model disagrees with Albarède and Juteau's (1984) finding of a constant time-integrated μ and is generally regarded as inconsistent with geological evidence (Milot et al., 2021). The model of Kramers and Tolstikhin (1997) assumes 43 paths of Pb evolution in the crust with μ and κ dynamically evolving in multiple reservoirs throughout Earth's history.

Some of these Pb evolution models are global in scope (e.g., Stacey et al., 1969; Cumming and Richards, 1975; Stacey and Kramers, 1975; Doe and Zartman, 1979; Zartman and Doe, 1981; Zartman and Haines, 1988; Kramers and Tolstikhin, 1997; Maltese and Mezger, 2020), whereas others are more regionally developed to make Pb growth predictions in geological terranes that are not well described by global models (e.g., Thorpe et al., 1992; Carr et al., 1995; Sun et al., 1996; Thorpe, 1999; Zametzer et al., 2022). Stacey and Kramers' (1975) two-stage model generally corresponds well with samples from many regions throughout Earth's history.

The idea of independently looking into ^{206}Pb and ^{208}Pb was raised by Patterson and Tatsumoto (1964). Albarède and Juteau (1984) introduced a graphical way of exploring Pb isotopic data. Their approach used a linearization – comparable to methods for Nd and Hf isotopes – in inverted space where ^{206}Pb/^{204}Pb, ^{207}Pb/^{204}Pb, or ^{208}Pb/^{204}Pb are plotted versus $e^{\lambda t}$ (with t being the accepted geological sample age). Sample Pb isotopic compositions are visualized relative to a regression line of galena samples published by Stacey and Kramers (1975), Cumming and Richards (1975), and Appel et al. (1978), indicating mantle compositions. However, the possibility of crustal contamination of galena needs to be pondered. Accordingly, Milot et al. (2021) considered this galena evolution line more representative of the upper continental crust. In any case, the power of this graphical approach lies in its independent look at ^{206}Pb, ^{207}Pb, and ^{208}Pb and the relative enrichment or depletion of these isotopes with respect to the global galena reference curve. Hartnady et al. (2022) extended this approach by associating a second stage of evolution to this graphical linearization, allowing the calculation of Pb model ages much like Nd and Hf two-stage model ages.

Combined, these approaches open up an additional dimension in the investigation of Pb sources and allow assessment of the degree of either mantle contribution or mixing with older crustal Pb through time.

3.3. Calculation of μ, ω, κ, and Pb model ages

Reforming equations Eq.1 and Eq.2 for the calculation of μ yields:

$$\mu_{64} = \frac{\left(\frac{206_{Pb}}{204_{Pb}}\right)_{t_2} - \left(\frac{206_{Pb}}{204_{Pb}}\right)_{t_1}}{\left(e^{\lambda_x \times t_1} - e^{\lambda_x \times t_2}\right)} \tag{4}$$

$$\mu_{74} = \frac{\left(\frac{207_{Pb}}{204_{Pb}}\right)_{t_2} - \left(\frac{207_{Pb}}{204_{Pb}}\right)_{t_1}}{\left(e^{\lambda_y \times t_1} - e^{\lambda_y \times t_2}\right)} \times 137.818 \tag{5}$$

Even though the calculation of one of the main derivative parameters of an isotopic system is an ostensibly fundamental procedure, no general guideline for the best way to calculate μ has been clearly established. With μ being a parameter present in the equations of both U-Pb decay schemes, the issue is in reaching the maximum possible agreement when interrogating both systems together with the choice of t_2. We are aware of four different published procedures for calculating a single μ value, representing both μ_{64} and μ_{74}. We briefly compare them here: 1) Albarède et al. (2012) calculated μ using a Pb model age for t_2 in Eq. 4 that is determined contemporaneously with μ based upon input ^{206}Pb/^{204}Pb ratios (and κ based upon ^{208}Pb/^{204}Pb ratios) and model parameters. 2) A very similar method of calculating μ was applied by Huston et al. (2017, 2019), performing the calculation of μ_{64} and μ_{74} iteratively as a function of time by slightly adjusting t_2 until Δμ converged to zero within an assigned level of tolerance. Approaches 1) and 2) are powerful for Pb isotopic data from samples of unknown age. However, the ages of samples in this study are well known or can be reasonably geologically constrained. 3) Armistead et al. (2021) used a known sample age t_2 to determine μ, whilst presuming a certain minimal degree of radiogenic ingrowth in the case that the data point was offset from the Pb evolution curve of the chosen model according to its μ value. This assumption may be a realistic approximation of the true geological situation for many crustal sampling media. 4) Zametzer et al. (2022) calculated μ_{64} and μ_{74} of analyzed granite K-feldspar based on known U-Pb zircon crystallization ages (t_2) and used the arithmetic mean of the two values to define one single μ. In this case, sample age and Pb model parameters are accommodated in the calculation and the difference between μ_{64} and μ_{74} ($\Delta\mu_{64}$-μ_{74}) may act as a proxy for the quality of the sampling medium and/or itself contain useful geological information.

We calculate μ, ω, and κ of all samples in our data set following methods 1), 2), 3), and 4) and report the results in Appendix A. Overall, the differences between μ calculated adopting approaches 1) to 4) are minimal (Appendix A). Nonetheless, samples which deviated substantially in calculated μ, dependent on the choice of calculation, imply isotopic ratios that are not appropriately represented by their chosen Pb evolution model. The Pb isotopic data compilation in this work represents various sampling media over an entire craton. Hence, for the discussions of temporal and spatial (lateral and vertical) trends seen in μ in the Yilgarn Craton we average μ_{64} and μ_{74} after Zametzer et al. (2022) and also consider $\Delta\mu_{64}$-μ_{74}.

The parameter ω can be determined through the following equation:

$$\omega = \frac{\left(\frac{208_{Pb}}{204_{Pb}}\right)_{t_2} - \left(\frac{208_{Pb}}{204_{Pb}}\right)_{t_1}}{\left(e^{\lambda_z \times t_1} - e^{\lambda_z \times t_2}\right)} \tag{6}$$

And κ results from:

$$\kappa = \frac{232_{Th}}{238_U} = \frac{\left(\frac{232_{Th}}{204_{Pb}}\right)}{\left(\frac{238_U}{204_{Pb}}\right)} = \frac{\omega}{\mu} \tag{7}$$

An additional parameter of the Pb isotope system is Pb model ages

that can provide model-based estimates of the crystallization or mineralization age of a sample, using its measured ^{206}Pb/^{204}Pb, ^{207}Pb/^{204}Pb, or ^{208}Pb/^{204}Pb ratios and specific Pb model parameters (e.g., Zartman and Wasserburg, 1969; Krishna Sinha and Tilton, 1973; Albarède et al., 2012; Huston et al., 2017; Milot et al., 2021; Armistead et al., 2021). We use equations of Albarède et al. (2012), Huston et al. (2017), and of Armistead et al. (2021) for the calculation of Pb model ages (Appendix A). We also determine the difference between the true sample age and its Pb model age (Δt; Huston et al., 2017). An alternative calculation method for Pb model ages (source ages) are linear regressions through data and the intercept of the regression line with the model curve (e.g., Kamber and Moorbath, 1998; Kamber et al., 2003). A prerequisite of this isochron approach is confidence in ascribing geological meaning to the spread of data defining the slope of the regression lines, which for individual spot laser data may reflect, to some degree, the effects of ^{204}Hg on ^{204}Pb (Delavault et al., 2018).

3.4. Pb evolution model choice

Zametzer et al. (2022) found that Maltese and Mezger's (2020) single-stage Pb evolution model for the Bulk Silicate Earth provided a much better approximation of Pb evolution in the Yilgarn Craton than Stacey and Kramers' (1975) two-stage model. The concept behind Maltese and Mezger's (2020) model is that the impact of a Mars-sized planetary body (Theia) into proto-Earth in the Hadean altered the U, Th, and Pb budget of silicate Earth. The start date, initial Pb compositions, and μ, ω, and κ of Maltese and Mezger's (2020) internally consistent model have been constrained to the Theia collision at 4498 Ma.

Early studies of initial Pb isotope compositions from feldspars of Archean gneisses in the North Atlantic Craton in Greenland were conducted by Moorbath et al. (1975) and Gancarz and Wasserburg (1977). These authors inferred that a model with at least two stages was required to well approximate the Pb evolution of Archean felsic plutonic rocks (see also Oversby, 1978). Important work by Oversby (1975, 1978) investigated Pb isotopic signatures from granite K-feldspar and their variability in the Kalgoorlie-Norseman area of the EGST and concluded that the Pb signatures must have multi-stage growth histories prior to magma generation. This aspect was also discussed by Zametzer et al. (2022), highlighting multiple Neoarchean pulses of mantle input in the Yilgarn Craton (e.g., Mole et al., 2019) that render single-stage Pb growth in Archean granite K-feldspar an over-simplification. Nonetheless, the single-stage growth curve based on Maltese and Mezger's (2020) model for the Bulk Silicate Earth (equations Eq.8 to Eq.10) appears to provide the most suitable framework to approximate Pb evolution in the Yilgarn Craton (Zametzer et al., 2022).

Zametzer et al. (2022) defined regional single-stage Pb evolution models for the Youanmi Terrane and the EGST in the Yilgarn Craton with initial Pb compositions and a start date corresponding with Maltese and Mezger's (2020) model but adjusted μ, ω, and κ values calculated from measured values of granite K-feldspar. Using the initial ^{206}Pb/^{204}Pb (9.345), ^{207}Pb/^{204}Pb (10.37), and ^{208}Pb/^{204}Pb (29.51) ratios and the start date (4498 Ma) after Maltese and Mezger (2020) and Zametzer et al. (2022), respectively, Eq.4, Eq.5, and Eq.6 can be modified to account for a single-stage calculation of μ and ω in the Yilgarn Craton:

$$\mu_{64} = \frac{\left(\frac{206_{Pb}}{204_{Pb}}\right)_{t_2} - 9.345}{\left(e^{\lambda_x \times 4498\ Ma} - e^{\lambda_x \times t_2}\right)} \tag{8}$$

$$\mu_{74} = \frac{\left(\frac{207_{Pb}}{204_{Pb}}\right)_{t_2} - 10.37}{\left(e^{\lambda_y \times 4498\ Ma} - e^{\lambda_y \times t_2}\right)} \times 137.818 \tag{9}$$

$$\omega = \frac{\left(\frac{^{208}Pb}{^{204}Pb}\right)_{t_2} - 29.51}{\left(e^{\lambda_z \times 4498 \ Ma} - e^{\lambda_z \times t_2}\right)} \tag{10}$$

A comparison of Zametzer et al.'s (2022) Yilgarn Pb models and Kramers and Tolstikhin's (1997) multi-stage models reveals that none of the six crustal and depleted mantle reservoirs modelled by Kramers and Tolstikhin (1997) corresponds satisfactorily with Yilgarn Craton Pb data. Thus, we use Zametzer et al.'s (2022) single-stage Pb evolution framework in this work as it has been shown to be regionally appropriate and allows a straightforward calculation of derivative parameters.

Furthermore, given that scatter around present-day (higher $^{206}Pb/^{204}Pb$) compositions (termed fossil or 'secondary isochrons' by Kamber et al., 2003) can be an issue in some ancient feldspars (e.g., Rosholt et al., 1973; Oversby, 1975, 1978; Ludwig and Silver, 1977; McNaughton and Bickle, 1987; Halla, 2005, 2014, 2018b) we define single initial Pb values for magmatic suites for the calculation of granite K-feldspar derivative parameters (Appendix A).

3.5. Pb isotopes and their variability applied to Archean crustal evolution

It has been shown by numerous workers that Pb isotopes are an important tool in studying Archean crustal generation, evolution, and recycling (see Kamber, 2015, and Halla, 2018b, for reviews). The Archean gneiss complex of SW Greenland was one of the first areas of interest for Pb isotopic studies of ancient continental crust (Moorbath et al., 1975; Gancarz and Wasserburg, 1977; Griffin et al., 1980; Kamber and Moorbath, 1998). Other cratons have also been investigated with Pb isotopes, often in conjunction with Nd and/or Hf (Oversby, 1976; Gariépy and Allègre, 1985; Wooden and Mueller, 1988; Carignan et al., 1993, 1995; Vervoort et al., 1994; Henry et al., 1998; Stevenson et al., 1999; Ayer and Dostal, 2000; Isnard and Gariépy, 2004; Halla, 2005; Bolhar et al., 2007; Ram Mohan et al., 2013; Champion and Huston, 2016; Petrus et al., 2016; Chapman et al., 2019, 2021; Hartnady et al., 2022). Several studies have used Pb isotope maps and cross-sections to understand crustal structure. For example, DeWolf and Mezger (1994), Henry et al. (1998), Stevenson et al. (1999), Ayer and Dostal (2000), Isnard and Gariépy (2004), and Arcuri and Dickin (2018) used Pb in conjunction with Nd to study Neoarchean mantle compositions and crustal growth, assimilation, contamination, and recycling in the Superior Province in Canada. Breaks in Pb isotopic maps in the Canadian Shield were documented by Carignan et al. (1993) from the Pontiac and Abitibi subprovinces, and by Petrus et al. (2016) from the edge of the Superior Province (supported by Hf isotopes). The location of a Pb isotopic break determined by Davis et al. (1996) from the Slave Craton differs from the location of a Nd isotopic boundary. Kamber et al. (2003, 2005) concluded that extreme $^{207}Pb/^{204}Pb$ ratios in Archean cratons – and therefore high-μ zones – could image ancient crustal nuclei.

Disentangling primary from secondary effects on Pb isotopes has been a repeated goal (Davis et al., 1996; Gruau et al., 1996; Isnard and Gariépy, 2004; Ram Mohan et al., 2013; Kamber, 2015; Petrus et al., 2016). For example, based on a review of galena and K-feldspar, spanning 3600 Ma to recent, Krishna Sinha and Tilton (1973) suggested a dominant mantle signal in the Pb isotopic data. In contrast, Pb isotopes in granite K-feldspar have been inferred to reflect crustal fractionation, which normally takes place in the mid to lower crust (e.g., Blaxland et al., 1979; Barbarin, 1990; Haldar and Tišljar, 2014; Halla, 2018b). Homogenization of Pb isotopic signatures in the lower crust through high-temperature fluids that predate the crystallization of granitic rocks has been proposed by McCulloch and Woodhead (1993). Zametzer et al. (2022) identified corresponding isotopic trends in Pb isotopes in granite K-feldspar and Nd isotopic signatures from the same dated rocks in the Yilgarn Craton. Specifically, more juvenile crust, as identified by Nd and Hf isotopes, in the Eastern Goldfields Superterrane was associated with lower model source average μ (= 8.72 ± 0.12) relative to a more evolved Youanmi Terrane (average μ = 8.93 ± 0.11). A correlation between Nd

signatures and Pb isotopic signatures from Pb-rich ores has been observed in several studies (Browning et al., 1987; Huston et al., 2005, 2014; Champion and Huston, 2016). These authors found a tendency of more juvenile Pb signatures (lower μ values) to follow younger Nd model ages in mineralized trends within the Yilgarn Craton.

4. Data set and methods

The Pb isotope data sets used in this work include: (i) newly acquired granite K-feldspar data (n = 8; Appendix B), integrated with (ii) granite K-feldspar (n = 27) and (iii) Pb-rich ore data (n = 320) compiled from literature sources (Appendix A). This compilation of Pb isotopic data (Appendix A) is contrasted with published zircon Hf (e.g., Wyche et al., 2012; Mole et al., 2014, 2019) and whole rock Nd (e.g., Champion and Sheraton, 1997; Cassidy and Champion, 2004; Champion, 2013).

The mineral content of eight disaggregated granite samples in epoxy rounds was determined using a Tescan Integrated Mineral Analyzer (TIMA; automated backscattered electron imaging and energy dispersive x-ray spectroscopy mineral identification). High-resolution backscattered electron (BSE) images of K-feldspar were acquired through a Hitachi TM3030 scanning electron microscope (SEM). Forty 50 μm diameter spots were set on K-feldspar grains in each individual sample after TIMA imaging, avoiding cracks, inclusions, and other visible heterogeneities. Twenty-three spots were ablated on one standard glass (NIST612; Hollocher and Ruiz, 1995; Pearce et al., 1997; Woodhead and Hergt, 2001) and 22 spots each on two feldspar reference materials in order to correct for Pb isotope fractionation via sample-standard bracketing. The primary reference material was 'Kf-SHAP' feldspar after Tyrrell et al. (2006). Measured and recommended values for the secondary 'Albany' K-feldspar reference material (Liebmann et al., 2022) are listed in Appendix B.

Laser ablation multi-collector inductively coupled plasma mass spectrometry (LA-MC-ICPMS; Nu Plasma II) in the John de Laeter Centre at Curtin University, Perth, was used to analyze $^{206}Pb/^{204}Pb$, $^{207}Pb/^{204}Pb$, and $^{208}Pb/^{204}Pb$ ratios of K-feldspar in the samples and reference materials. Data were reduced in the software *iolite 4.3.8* (Paton et al., 2011). Isotopic ratios of Pb corrected for isobaric interference with Hg on mass 204 were calculated from the measured isotopes and are reported together with approximate Pb concentrations and the $^{204}Hg/^{204}Total$ (= Pb + Hg) ratio. The Hg interference correction was carried out in conjunction with an assumed relative $^{204}Hg/^{202}Hg$ abundance of 0.22988 (Kent, 2008) in order to determine ^{204}Hg that was subtracted from ^{204}Pb (Delavault et al., 2018). Internal and external error sources were integrated into the propagation of absolute 2σ uncertainties in quadrature.

We report individual spot Pb isotope ratios measured in the samples and reference materials together with absolute propagated 2σ uncertainties, approximate Pb content, and $^{204}Hg/^{204}Total$ ratios in Appendix B. The calculated $^{204}Hg/^{204}Total$ ratio quantifies Hg interference in the analyzed samples and provides a filtering criterion for granite K-feldspar Pb isotopic data (all data points with $^{204}Hg/^{204}Total$ ratio ≥ 5 % are omitted from further discussion), together with low Pb content (Pb concentration ≤ 10 ppm) and heterogeneous ablation response resulting in very large absolute propagated uncertainties (≥ 0.2 for $^{206}Pb/^{204}Pb$ and $^{207}Pb/^{204}Pb$ and absolute propagated uncertainty ≥ 0.4 for $^{208}Pb/^{204}Pb$). These filtering criteria account for analyses related to cracks, alteration, and inclusions that affect primary Pb isotopic signatures (Zametzer et al., 2022). Remaining primary data are used to calculate median $^{206}Pb/^{204}Pb$, $^{207}Pb/^{204}Pb$, and $^{208}Pb/^{204}Pb$ ratios for eight granite samples based on the K-feldspar separate analyses that are listed in Appendix B.

The eight newly presented granite K-feldspar samples have been dated via sensitive high resolution ion microprobe (SHRIMP) U-Pb zircon geochronology (Nelson, 1997a, 1997b, 1998, 1999; Lu et al., 2016). The U-Pb zircon data set of sample 142802 shows two distinct groups of analyses that allow the interpretation of either 2801 ± 10 Ma

or 2668 ± 15 Ma as the igneous crystallization age (Nelson, 1997a). We treat 2668 ± 15 Ma as the granite crystallization age of sample 142802. Granite whole rock geochemical data for seven out of eight samples can be attained from the Geological Survey of Western Australia (https://geoview.dmp.wa.gov.au/geoview/).

Ore mineral Pb isotope data were collated from the literature, including those which form part of the national Pb isotope map of Australia (Huston et al., 2019). This compilation comprises common Pb isotopic data from Pb-rich ores – galena in particular and also other sulfides and tellurides like pyrite, chalcopyrite, arsenopyrite, sphalerite, pyrrhotite, pentlandite, cosalite, twinnite, altaite, and melonite (e.g., Browning et al., 1987; Huston et al., 2014). The Pb isotopic data from Pb-rich ores are subdivided into three different deposit types: gold ($n =$ 220), volcanic-hosted massive sulfides (VHMS; $n = 62$), and komatiite-hosted Ni sulfides ($n = 38$; see Appendix A).

The compiled $^{206}Pb/^{204}Pb$, $^{207}Pb/^{204}Pb$, and $^{208}Pb/^{204}Pb$ ratios from Pb-rich ores and from granite K-feldspar were used to calculate average μ, ω, and κ values, following equations Eq.8, Eq.9, and Eq.10. Additional derivative parameters that have been determined for each individual sample are Pb model ages, following Albarède et al. (2012), Huston et al. (2017), and Armistead et al. (2021), and Δt which is the difference between the true sample and its Pb model age (see Huston et al., 2017). All compiled Pb isotope data sets were filtered using the same criterion of Zametzer et al. (2022) for U and/or Th concentration ≥ 0.5 ppm (if reported). Data were also filtered for abnormal ratios of $^{206}Pb/^{204}Pb$ and $^{207}Pb/^{204}Pb$ reflecting radiogenic ingrowth through U-bearing inclusions (typically if $^{206}Pb/^{204}Pb \geq {}^{207}Pb/^{204}Pb$), large uncertainties reflecting heterogeneous ablation response (≥ 0.2 for $^{206}Pb/^{204}Pb$ and $^{207}Pb/^{204}Pb$ and ≥ 0.4 for $^{208}Pb/^{204}Pb$), and low Pb content (≤ 10 ppm).

The known SHRIMP U-Pb zircon crystallization age substitutes for t_2 in equations Eq.8, Eq.9, and Eq.10 for granite K-feldspar samples where available (e.g., Wang et al., 1993; Yeats et al., 1996; Nelson, 1997a, 1997b, 1998, 1999; Qiu and McNaughton, 1999; Qiu et al., 1999; Fletcher and McNaughton, 2001; Dunphy et al., 2003; Zametzer et al., 2022), and literature mineralization ages are used for Pb-rich ores. The procedure to determine t_2 is given in Appendix C.

The Yilgarn Craton Pb isotopic data compilation (overall $n = 355$) was sorted by sampling media (minerals and rock types) and four different chemical process groups (granite K-feldspar, ore minerals from three different deposit types) to structure the discussion around vertical and lateral crustal trends (see also Tables 1 and 2, Fig. 2, and Appendix A).

In order to quantify the heterogeneity of possible Pb sources, we calculated the Shannon-Weaver diversity index (Shannon and Weaver, 1949; Spellerberg and Fedor, 2003) for $^{206}Pb/^{204}Pb$, $^{207}Pb/^{204}Pb$, and $^{208}Pb/^{204}Pb$ ratios, and for calculated Pb model ages and Δt of all chemical process groups. The Shannon-Weaver index is a frequently applied statistical tool, particularly in ecology, but has been used in geological contexts in lithological compositional analysis (Smosna et al., 1999), as well as in assessing the heterogeneity of detrital zircon age spectra (Gartmair et al., 2021). A higher index value correlates with greater diversity (Shannon and Weaver, 1949; Spellerberg and Fedor, 2003). This index performs a normalization of data from groups with very different statistical population sizes. Bin widths have to be defined and are identical for all groups of data that are being directly compared to each other (individual Pb isotope ratios, Pb model ages, and Δt). Bin widths used for our data set are 0.25 ($^{206}Pb/^{204}Pb$ ratios), 0.20 ($^{207}Pb/^{204}Pb$ ratios), 1.40 ($^{208}Pb/^{204}Pb$ ratios), and 250 (Pb model ages, Δt). Related bin value ranges are 10.0–15.5 ($^{206}Pb/^{204}Pb$ ratios), 14.0–15.6 ($^{207}Pb/^{204}Pb$ ratios), 30.8–36.4 ($^{208}Pb/^{204}Pb$ ratios), 2000–7500 (Pb model ages), and −4500–1000 (Δt).

5. Results

A laser ablation protocol for Pb isotopes may offer some advantages in screening for secondary effects, through for example the identification of unintentional ablation of low-Pb zones or U- and Th-bearing inclusions (e.g., Tyrrell et al., 2006, 2012; Hartnady et al., 2022). In order to also exclude the possibility of partial ablation of unsupported radiogenic Pb in granite K-feldspar, acid-leaching, e.g., with strong HCl and cold HF, could be used prior to laser ablation analysis (e.g., Ludwig and Silver, 1977). In this work, we apply filtering criteria similar to that used in Zametzer et al. (2022). Time-resolved Pb isotopic counts display characteristic signals for primary K-feldspar, low-Pb perthite lamellae, and explosive removals during ablation (Fig. 3). Recognition of inconsistencies in the time-resolved data allows filtering to exclude analyses likely reflecting radiogenic ingrowth (in the form of high $^{206}Pb/^{204}Pb$ ratios) and/or alteration (Fig. 3; see also Appendix B). Only primary data after filtering are used for the calculation of median $^{206}Pb/^{204}Pb$, $^{207}Pb/^{204}Pb$, and $^{208}Pb/^{204}Pb$ ratios, which precedes the derivation of μ, ω, κ, Pb model ages, and Δt. Therefore, the median Pb isotope ratios most conservatively can be interpreted as upper limits for initial Pb isotope ratios.

The geochemistry of seven whole rock granite samples (from which the analyzed K-feldspar splits were derived) is examined through the aluminium saturation index (ASI) that evaluates the deficit of alkali elements over Al_2O_3 which, for most naturally non-peraluminous igneous rocks, is interpreted as reflecting alteration of feldspar (Zen, 1986; Witt and Davy, 1997b; Fig. 4). The data from the K-feldspar samples plot within the ASI versus loss on ignition (LOI) field of "least altered" Yilgarn Craton granites (Fig. 4). However, one of the samples investigated in this work has a more moderate LOI (~3 pct). Nonetheless, this sample's K-feldspar petrographically appears little altered. Exclusion of this sample's data results in no meaningful change to the regional nor temporal Pb isotopic patterns.

Granite K-feldspar ($n = 35$) is the sampling medium with the highest median μ (8.86), whereas galena samples ($n = 166$) have the lowest median μ (8.67) and ω (36.48; Table 1). Pyrite ($n = 102$; median μ = 8.76; median ω = 37.04) and other Pb-rich ore minerals ($n = 29$; median μ = 8.72; median ω = 37.33) yield similar values (Table 1). Other sampling media include carbonate, gossan, and sulfide ore whole rock samples ($n = 23$) with a median μ of 8.78 and the highest median ω of 37.51 in this data set (Table 1).

Calculated median μ values of different chemical process groups range from 8.51 (VHMS ores) to 8.86 (granite K-feldspar), median ω from 35.61 (VHMS ores) to 37.98 (komatiite-hosted Ni sulfide ores), and

Table 1
Calculated medians of Pb isotope derivative parameters for the whole data set sorted by sampling media and chemical process groups.

Sampling medium	n (overall)	μ	Δμ₆₄-μ₇₄	ω	κ	Pb model age [Ma]	Δt [Ma]
Granite K-feldspar	35	8.86	0.09	37.23	4.22	2631	38
Galena	166	8.67	−0.04	36.48	4.16	2663	−18
Pyrite	102	8.76	0.12	37.04	4.23	2625	48
Other Pb-rich ore minerals	29	8.72	0.16	37.33	4.26	2636	64
Others (Carbonate, gossan, sulfide ore whole rock)	23	8.78	0.12	37.51	4.28	2654	51
Chemical Process Group							
Komatiite-hosted Ni sulfide ores	38	8.80	0.18	37.98	4.30	2641	73
Granite K-feldspar	35	8.86	0.09	37.36	4.22	2631	38
Gold ores	220	8.76	0.02	36.83	4.18	2637	7
VHMS ores	62	8.51	−0.04	35.61	4.20	2720	−20

Table 2
Calculated medians of Pb isotope derivative parameters for the data set, subdivided into Youanmi Terrane and Eastern Goldfields Superterrane, and sorted by sampling media and chemical process groups.

Sampling medium	n (Youanmi Terrane)	μ	$\Delta\mu_{64}$-μ_{74}	ω	κ	Pb model age [Ma]	Δt [Ma]	n (EGST)	μ	$\Delta\mu_{64}$-μ_{74}	ω	κ	Pb model age [Ma]	Δt [Ma]
Granite K-feldspar	14	9.04	0.15	38.27	4.26	2601	63	21	8.77	0.07	36.74	4.18	2642	33
Galena	45	8.61	−0.16	36.36	4.20	2720	−64	121	8.75	−0.02	36.54	4.16	2658	−7
Pyrite	45	8.81	0.08	37.30	4.20	2637	34	57	8.75	0.12	37.00	4.25	2622	50
Other Pb-rich ore minerals	3	9.46	1.10	39.96	4.22	2223	439	26	8.71	0.08	37.27	4.26	2639	35
Others (Carbonate, gossan, sulfide ore whole rock)								23	8.78	0.12	37.51	4.28	2654	51
Chemical Process Group														
Komatiite-hosted Ni sulfide ores	8	10.19	1.76	44.05	4.38	2265	625	30	8.77	0.15	37.59	4.28	2643	62
Granite K-feldspar	14	9.04	0.15	38.27	4.26	2601	63	21	8.77	0.07	36.74	4.18	2642	33
Gold ores	63	8.67	−0.08	36.47	4.20	2675	−32	157	8.78	0.05	37.09	4.17	2624	21
VHMS ores	22	8.52	−0.15	35.82	4.19	2993	−58	40	8.51	−0.04	35.37	4.20	2714	−18

median κ from 4.18 (gold ores) to 4.30 (komatiite-hosted Ni sulfide ores; Table 1 and Fig. 5). Subdividing the chemical process groups into sample locations from west and east of the Ida Fault reveals a trend from higher μ and ω values in the Youanmi Terrane across the Ida Fault to lower values in the EGST in all groups apart from gold ores (Table 2 and Fig. 5). A minor exception is the median μ value of ores from VHMS deposits that is almost identical in the Youanmi Terrane (8.52) and the EGST (8.51; Table 2 and Fig. 5). Mean μ is higher in VHMS ore samples from west of the Ida Fault (8.67 vs. 8.42 in EGST samples). The VHMS ores have the lowest median μ and ω values in our data set (Tables 1 and 2 and Fig. 5). The highest median μ (10.19), ω (44.05), and κ (4.38) are seen in komatiite-hosted Ni sulfide ores from the Youanmi Terrane (Table 2). In the EGST, median μ and ω values of gold ores, granite k-feldspar, and komatiite-hosted Ni sulfide ores lie within a comparable range (Table 2). Overall, calculated mean μ, ω, and κ are very similar to the medians.

A small difference in median κ between higher values west and lower values east of the Ida Fault is recorded in granite K-feldspar (4.26 vs. 4.18), in ores from gold deposits (4.20 vs. 4.17), and also in ores from komatiite-hosted Ni sulfides (4.38 vs. 4.28; Table 2 and Fig. 5). Median κ does not reflect this weak trend in ores from VHMS deposits (4.19, 4.20) on either side of the fault (Table 2 and Fig. 5).

Medians of the parameter $\Delta\mu_{64}$-μ_{74} are small for granite K-feldspar (0.09), galena (−0.04), pyrite (0.12), other Pb-rich ore minerals (0.16), and other sampling media (0.12; Table 1). No trend across the Ida Fault is recorded in $\Delta\mu_{64}$-μ_{74} in different sampling media or chemical process groups (Table 2). The process group with the largest $\Delta\mu_{64}$-μ_{74} are komatiite-hosted Ni sulfide ores from the Youanmi Terrane (1.76).

Calculated median Pb model ages of granite K-feldspar (2631 Ma), galena (2663 Ma), pyrite (2625 Ma), other Pb-rich ore minerals (2636 Ma), and other sampling media (2654 Ma) fall in a very similar range (Table 1). Median Pb model ages are older for VHMS ore samples (Youanmi Terrane: 2993 Ma; EGST: 2714 Ma) than for the other process groups (Table 2). Komatiite-hosted Ni sulfide ores from the Youanmi Terrane have the youngest median Pb model ages (2265 Ma), while komatiite-hosted Ni sulfide ores from the EGST (2643 Ma), gold ores (Youanmi Terrane: 2675 Ma; EGST: 2624 Ma), and granite K-feldspar (Youanmi Terrane: 2601 Ma; EGST: 2642 Ma) are comparable with no general terrane-scale tendency across the Ida Fault (Table 2).

The difference between known or constrained samples ages and Pb model ages, as expressed by the parameter Δt (Huston et al., 2017), shows an overall distribution in sampling media akin to $\Delta\mu_{64}$-μ_{74} with values between −18 (galena) and 64 (other Pb-rich ore minerals) for the other sampling media (Table 1). The absolute value of Δt is greater in the Youanmi Terrane than in the EGST in all process groups (Table 2).

Differences between Pb isotope derivative parameters of different sampling media and chemical process groups are greater in the Youanmi Terrane with respect to more homogeneous values in the EGST (Table 2). Owing to the rather subtle overall nature of changes in our data set, a statistical analysis of the variety of Pb isotope ratios as well as of Pb model ages and Δt facilitates more robust interrogation of data significance. A Shannon-Weaver diversity/heterogeneity test (Shannon and Weaver, 1949; Spellerberg and Fedor, 2003) yields the highest values, and thus the largest diversity, for $^{206}Pb/^{204}Pb$, $^{207}Pb/^{204}Pb$, and $^{208}Pb/^{204}Pb$ ratios, Pb model ages, and Δt in the gold ore samples and in komatiite-hosted Ni sulfide ore samples from the Youanmi Terrane (Fig. 6). The Pb isotope ratios and derivative parameters of VHMS ores, granite K-feldspar, and komatiite-hosted Ni sulfide ores from the EGST have similar diversity metrics (Fig. 6). The $^{206}Pb/^{204}Pb$ and $^{207}Pb/^{204}Pb$ ratios are generally more diverse than $^{208}Pb/^{204}Pb$ ratios, with the exception of granite K-feldspar samples from the EGST (Fig. 6). A trend towards lower variability in the EGST is seen in $^{206}Pb/^{204}Pb$ and $^{208}Pb/^{204}Pb$ ratios, as well as in Pb model ages, and Δt in all process groups but gold ores (Fig. 6).

The bulk of the data set used in this study plots between the 'depleted mafic crust' and 'upper crust' endmembers of McNaughton and Groves' (1996) Pb source model for the EGST in a $^{207}Pb/^{204}Pb$ vs. $^{206}Pb/^{204}Pb$ plot (Fig. 7). None of the multi-stage Pb evolution curves for different crustal reservoirs by Kramers and Tolstikhin (1997) can fully describe isotopic variability evident in the Yilgarn Craton (Fig. 7). Nonetheless, the 'erosion mix' multi-stage model (Kramers and Tolstikhin, 1997) closely overlaps Zametzer et al.'s (2022) single-stage curve for the EGST. However, Pb model ages according to the 'erosion mix' curve (Kramers and Tolstikhin, 1997) still indicate a significant offset from the known sample ages (Fig. 7). This age offset also applies to model ages calculated with the 'upper mantle' and 'young upper crust' curves for data from the Teutonic Bore deposit and to model ages calculated with the 'old upper crust' curve (Kramers and Tolstikhin, 1997) for data from the Norseman area (Fig. 7).

In thorogenic Pb space ($^{208}Pb/^{204}Pb$ vs. $^{206}Pb/^{204}Pb$) Yilgarn Craton data largely fall between the Pb evolution curves for the Youanmi Terrane and the EGST (Fig. 8). This plot indicates a relatively systematic distribution of data sorted by chemical process groups with VHMS ore and komatiite-hosted Ni sulfide samples plotting towards older thorogenic Pb sources (~3050–2800 Ma) in relation to the Pb evolution models, and gold ores and granite K-feldspar mostly straddling the model curves between ~2700–2600 Ma (Fig. 8). Distinct groups in the thorogenic Pb evolution diagram are VHMS ore samples from the Golden Grove and Mount Gibson deposits at ~3050 Ma and VHMS ores from the Teutonic Bore deposit at ~2800 Ma (Fig. 8).

A graphical linearization following Albarède and Juteau (1984) shows a deficit in ^{206}Pb and ^{208}Pb in VHMS ores relative to the other chemical process groups (Figs. 9a and 10) and also a depletion in ^{207}Pb
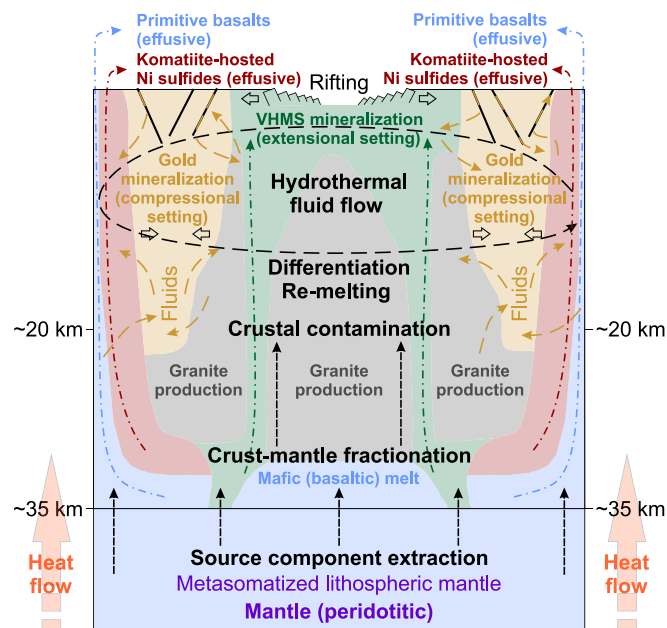
Fig. 2. Idealized concept of Pb sources, 'chemical communication' (U, Th, and Pb transfer; material exchange), and processes throughout the entire crustal column using the example of the Yilgarn Craton's continental crust. An overall large-scale driver of chemical processes and isotopic fluxes is heat flow from the lower mantle to the upper mantle and to crustal reservoirs. The crust-mantle boundary lies ~35 km deep in most parts of the Yilgarn Craton. The maximum depth indicated in the crustal column and the upper mantle refers to the location at which the Pb is sourced in the following (colour-coded) chemical process groups: 1) The upper mantle consists of asthenospheric and lithospheric mantle, the latter of which represents the residual after melt extraction and is often metasomatized. Primitive basalts would be expected to carry a Pb signature that was initially sourced from the metasomatized mantle. In our data set, a Pb mantle signal is best approximated by volcanic-hosted massive sulfide (VHMS) ores. 2) Granites crystallized from lower to mid crustal melts and document processes like differentiation and re-melting of protoliths; consequently, their Pb isotopic signature is that of the lower to middle crust. A modification of the Pb isotopic signal in granite K-feldspar through granite fractionation and/or crustal contamination is very likely. 3) Different ore deposits mineralize through various processes and in different geodynamic settings; thus, the related ore minerals may represent various and mixed Pb sources. Even though komatiite-hosted Ni sulfides sit in extrusive rocks, Pb isotopic signatures can be linked to upper mantle and/or lower crustal levels, as they formed in extensional settings with rapid ascent of ultramafic melts. Komatiitic melts are likely to pick up Pb along their emplacement pathways through thermal erosion of the crustal substrate. Gold mineralization takes place in a range of mid to upper crustal depths with variable hydrothermal fluid flow that can potentially blur Pb isotopic signatures through leaching of Pb from the surrounding rocks and fluid mixing. Hence, the Pb isotopic signature of these deposits will be an indication of the mixture of rock types in the middle to upper crust within the source region sampled by the ore fluids. This will involve rocks whose original source was from the mantle (e.g., basalts), the lower to middle crust (granites and associated volcanic rocks) and the upper crust (sediments). The formation of gold deposits and the peak of gold mineralization events in the Yilgarn Craton is typically associated with compressional or transpressional tectonic environments. Mineralization in VHMS deposits is confined to upper crustal levels and extensional geodynamic settings (rifting). Even though VHMS deposits are now part of the Yilgarn Craton's continental crust, mineralization initially happened on seafloor hydrothermal systems. The Pb source area of VHMS deposits is the upper crust, which will constitute a mixture of basalts (derived from the upper mantle), felsic volcanic rocks, and sediments. The strong mafic and mantle-derived component in the Pb sources makes VHMS ores a comparatively primitive chemical process group. (For interpretation of the references to colour in this figure legend, the reader is referred to the web version of this article.)

(Fig. 9b). Granite K-feldspar and gold ores have very similar Pb isotopic ratios overall and tend to have lower $^{206}Pb/^{204}Pb$ ratios than Albarède and Juteau's (1984) reference line for global galenas. In inverted $^{207}Pb/^{204}Pb$ and $^{208}Pb/^{204}Pb$ space granite K-feldspar and gold ore samples align closely to this reference linearization (Fig. 9). Granite K-feldspar $^{206}Pb/^{204}Pb$, $^{207}Pb/^{204}Pb$, and $^{208}Pb/^{204}Pb$ ratios are higher in Youanmi Terrane samples in comparison to EGST samples (Figs. 9, 10, and 11). Komatiite-hosted Ni sulfide ores from the Youanmi Terrane plot above Albarède and Juteau's (1984) reference line for all three Pb isotopes, while EGST samples show a good agreement with the reference line (Figs. 9 and 10).

There is a general trend to a slight deficit in ^{206}Pb and a subtle enrichment in ^{207}Pb (compare Pb-in-granite-K-feldspar samples from Zametzer et al., 2022), while most samples investigated here generally align relatively closely to the reference line for global galenas in inverted $^{208}Pb/^{204}Pb$ space (Fig. 10).

Specifically, granite K-feldspar samples from the Youanmi Terrane show a tendency towards higher $^{207}Pb/^{204}Pb$ (Fig. 11b) and $^{208}Pb/^{204}Pb$ ratios (Fig. 11c) and to a lesser extent also towards higher $^{206}Pb/^{204}Pb$ ratios (Fig. 11a) with younger crystallization ages. The negative correlation between granite crystallization age and $^{207}Pb/^{204}Pb$ ratios ($p = 0.041$ [95.9 % conf.], $r^2 = 0.30$; Fig. 11b) and $^{208}Pb/^{204}Pb$ ratios ($p = 0.009$ [99.9 % conf.], $r^2 = 0.45$; Fig. 11c) is statistically significant in a linear least squares regression. The same apparent negative correlation is not visible in EGST granite K-feldspar samples (Fig. 11).

6. Discussion

6.1. Approximating the mafic magma source: the upper mantle

Components that build up source rocks from which the continental crust may grow are extracted from the mantle. This extraction is a process that is defined by partial melting and fractional crystallization, driven by the cooling of the melt and by the individual crystallization and melting temperatures of different minerals (Champion and Sheraton, 1997; Laurent et al., 2013). A partial melt from the upper mantle would usually be expected to be of basaltic (low-Th basalt-like; Pearce, 2008; Barnes et al., 2012; Smithies et al., 2018a) composition (Fig. 2). The daughter isotopes of Nd and Hf fractionate into melts more strongly than their parent isotopes of Sm and Lu, which makes the Sm-Nd and Lu-Hf isotope systems suitable tracers of the timing of extraction of source components from the mantle into developing crustal melts (Kinny and Maas, 2003; Hawkesworth and Kemp, 2006b). Several Sm-Nd (e.g., Champion and Sheraton, 1997; Cassidy and Champion, 2004; Champion, 2013) and Lu-Hf (e.g., Wyche et al., 2012; Mole et al., 2014, 2019) isotopic studies and maps of the Yilgarn Craton show a clear distinction between older model ages (average literature $T^2_{DM} \approx 3200$ Ma), and thus a higher proportion of older crustal components, in the Youanmi Terrane, and on average approximately 200 Ma younger model ages (average literature $T^2_{DM} \approx 3000$ Ma), and thus a higher proportion of juvenile mantle input, in the EGST.

Aspects of mantle geochemistry can also be deduced from Pb isotopes (e.g., Patterson and Tatsumoto, 1964; Hofmann, 1988, 1997; Castillo et al., 2018; Pettke et al., 2018; Doucet et al., 2020). The strongly lithophile nature of U and its ongoing fractionation into the crust (Taylor and McLennan, 1985; Hofmann, 1988, 1997) results in a continuous change of the mantle Pb isotopic composition through time. Moorbath and Taylor (1981) determined an average μ value of 7.75 for the Archean mantle. Even higher Archean time-integrated mantle μ (8–9) has been suggested (Maltese and Mezger, 2020). Furthermore, DeWolf and Mezger (1994) and Maltese and Mezger (2020) inferred only small differences in μ and ω between mantle and continental crust reservoirs in the Archean. White (1993) calculated the present-day μ value of Earth's mantle as low (< 6) compared to past values. Low μ and ω values are interpreted to represent the residue after extraction and fractionation of U and Th into the crust and can therefore potentially
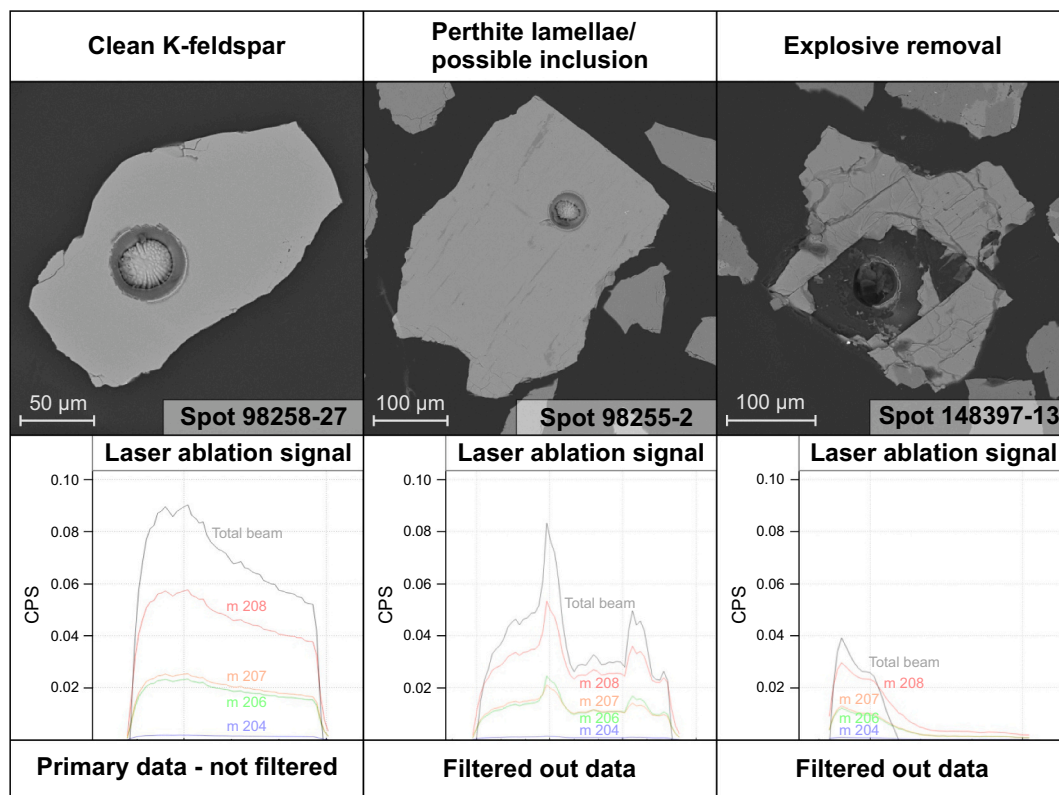
Fig. 3. Backscattered electron (BSE) images and related time-resolved laser ablation signals exemplify 'clean' K-feldspar, partial ablation of perthite lamellae and possible downhole ablation of inclusions in K-feldspar, and explosive removal of K-feldspar through the laser beam (and fractures). Laser ablation signals shown include the total beam in counts per second (CPS) and signals for Pb isotope masses 204, 206, 207, and 208. Filtering protocols for Pb isotopic data applied in this work will result in removal of individual spot analyses that represent the ablation of perthite lamellae and explosive removals.
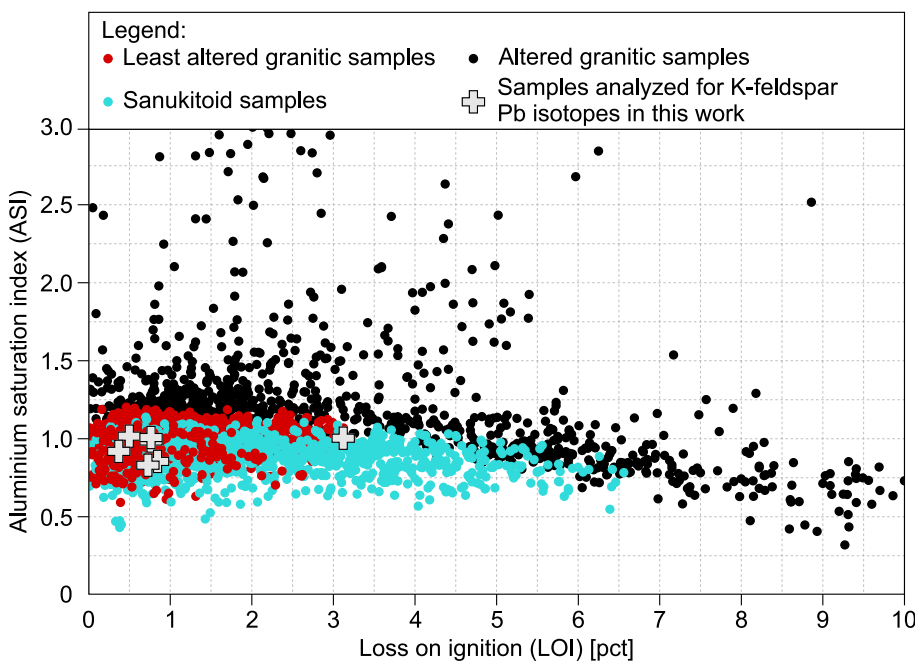
Fig. 4. Aluminium saturation index (ASI (molar) = $Al_2O_3/(CaO + K_2O + Na_2O)$; Zen, 1986) versus loss on ignition (LOI) plot for an encompassing Yilgarn Craton granite data set as provided by the Geological Survey of Western Australia (GSWA). Altered granitic samples are indicated by black circles, hornblende diorites (sanukitoids) by blue circles, while least altered granitic samples are indicated by red circles. An LOI cut-off grade of ~3 pct is used for 'least altered granitic rocks' in the GSWA data set, although many samples with >3 pct LOI retain typical 'igneous' mantle-normalized trace element (rare earth elements and high field-strength element) patterns. Granite K-feldspar samples investigated in this work (grey cross symbols) fall in the least altered compositional range. (For interpretation of the references to colour in this figure legend, the reader is referred to the web version of this article.)

reflect derivation from a depleted mantle resulting from the formation of continental crust (Hofmann, 1988, 1997).

The least modified Pb isotopic representation of possible mantle signatures in the Yilgarn Craton data set are ores from volcanic-hosted massive sulfides (VHMS) which are deposits characterized by an enrichment of metals like Zn, Cu, and Ag that formed in extensional settings with pronounced crustal thinning (see Franklin et al., 2005, for a review). Although now trapped as part of the continental crust, the formation of VHMS deposits is thought to be confined to seafloor hydrothermal systems, assigned to shallow crustal levels (Franklin et al.,
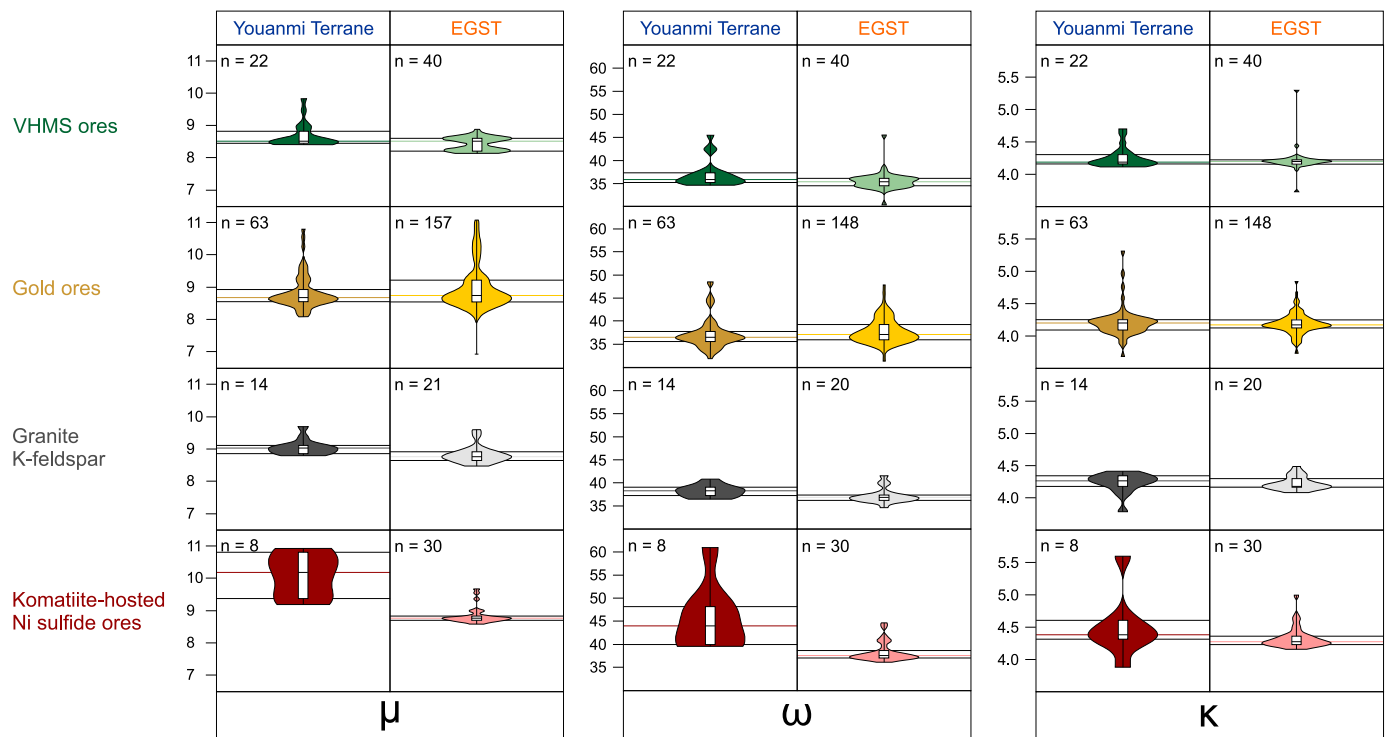
Fig. 5. Violin plots with median line and 75% and 25% percentiles for four chemical process groups and parameters μ, ω, and κ. Median μ and ω values are higher in the Youanmi Terrane relative to the EGST in all process groups but gold ores. A similarly strong trend is not recorded in κ. Granite K-feldspar and komatiite-hosted Ni sulfide ores show trends to higher κ in the Youanmi Terrane, whereas median κ values are comparable in gold ores and VHMS ores. Sample numbers of μ and ω/κ of gold ores and granite K-feldspar from the Eastern Goldfields Superterrane are not identical because of the lack of $^{208}Pb/^{204}Pb$ ratios for nine samples (gold ores) and one sample (granite K-feldspar), respectively, in the literature sources from which the Pb ratios were compiled. (For interpretation of the references to colour in this figure legend, the reader is referred to the web version of this article.)

2005; Huston et al., 2010; Piercey, 2011). Huston et al. (2014) demonstrated that low-μ zones in Archean cratons correspond with extensional paleosettings and used this isotopic feature as a targeting criterion for Archean VHMS deposits. The Yilgarn Craton is poorly endowed with VHMS deposits compared to other Archean crustal segments like the Abitibi and Wawa subprovinces of the Superior super-craton in Canada (Gariépy and Allègre, 1985; Thorpe, 1999; Huston et al., 2014; Hollis et al., 2015, 2017) – a fact that indicates that rifting and thinning of the crust may have been limited prior to a switch back to compressional processes. The thin crust in extensional regimes allows the rapid ascent of less contaminated mafic melts from deeper crustal levels (Piercey, 2011). A limited role for crustal contamination is consistent with our results for Pb-rich ores from VHMS deposits that yield low median μ (8.51) and ω (35.61; Tables 1 and 2 and Fig. 5). Hence, low μ and ω values suggest a strong mantle-derived basalt component in the VHMS ore Pb signatures (Fig. 2). Median $\Delta\mu_{64}$-μ_{74} of VHMS ores is small (−0.04; Table 1), backing up the data quality of this chemical process group. The oldest median Pb model age (2720 Ma; Table 1) and a deficit in ^{206}Pb (Fig. 9a), ^{208}Pb (Fig. 10), and even in ^{207}Pb (Fig. 9b) also suggests a stronger mantle Pb signature relative to other chemical process groups.

The two distinct peaks visible in the violin plots for μ (Fig. 5) display sample groups from different VHMS camps (Fig. 1) with characteristic differences in median μ (and also ω). The Teutonic Bore VHMS camp (Barrote et al., 2020a) samples have significantly lower μ values (median and mean ~8.2; Fig. 7) than ore samples from the Nimbus VHMS deposit (Barrote et al., 2020b) and the Duketon prospect (median and mean μ ~8.6). Based on the calculation through a regionally appropriate Pb evolution model for the Yilgarn Craton VHMS ore Pb isotopic data approximate the Neoarchean mantle μ between ≤ ~8.13 (most juvenile ESGT data) and ≤ ~8.41 (Youanmi Terrane) and mantle ω between ≤ ~30.31 (EGST) and ≤ ~34.58 (Youanmi Terrane; Appendix A). Since μ

and ω results from the Teutonic Bore camp closely approximate assumed mantle signatures (Huston et al., 2014), we speculate that Teutonic Bore records a stronger degree of extension or more direct mantle tapping structures relative to other areas with VHMS mineralization. The higher-μ mineralized zones at Nimbus and Duketon are located along terrane boundaries (Fig. 1) and could represent extensional settings that rapidly switched back to compressional or transpressional regimes (e.g., failed rifts).

6.2. Granitic magma source: the middle to lower crust

K-feldspar Pb isotopic data from granite samples display higher median μ, ω, κ, and Δt in samples from west of the Ida Fault relative to samples from east of the Ida Fault (Table 2 and Figs. 5 and 6). Granite crystallization ages do not correlate with Pb isotope derivative parameters (Zametzer et al., 2022). As demonstrated in Appendix D, which includes calculations for our entire data set, a timing difference of 200 Ma (the average difference between Nd and Hf model ages west and east of the Ida Fault) can account for the relatively small magnitude of the difference in μ and ω (Δμ ≈ 0.3 and Δω ≈ 1.3). Hence, what is recorded in the difference in μ, ω, and Δt across the Ida Fault likely is the timing of initial extraction of source material from the mantle that the granites eventually evolved from (Appendix D) – analogous to Nd and Hf isotopic signatures. A compositional difference in U/Pb and Th/Pb of the granite bulk source comprising a higher proportion of old crustal material in the Youanmi Terrane and more juvenile input in the EGST is a conceivable influence on the Pb signatures as well. Furthermore, the greater dichotomy of input Pb ratios (excluding $^{207}Pb/^{204}Pb$), Pb model ages, and Δt (Fig. 6) documents a more evolved crust in the older Youanmi Terrane with respect to a more juvenile, and therefore generally more homogeneous EGST. Higher $^{206}Pb/^{204}Pb$, $^{207}Pb/^{204}Pb$, and $^{208}Pb/^{204}Pb$ ratios are observed in Youanmi Terrane granite K-feldspar samples
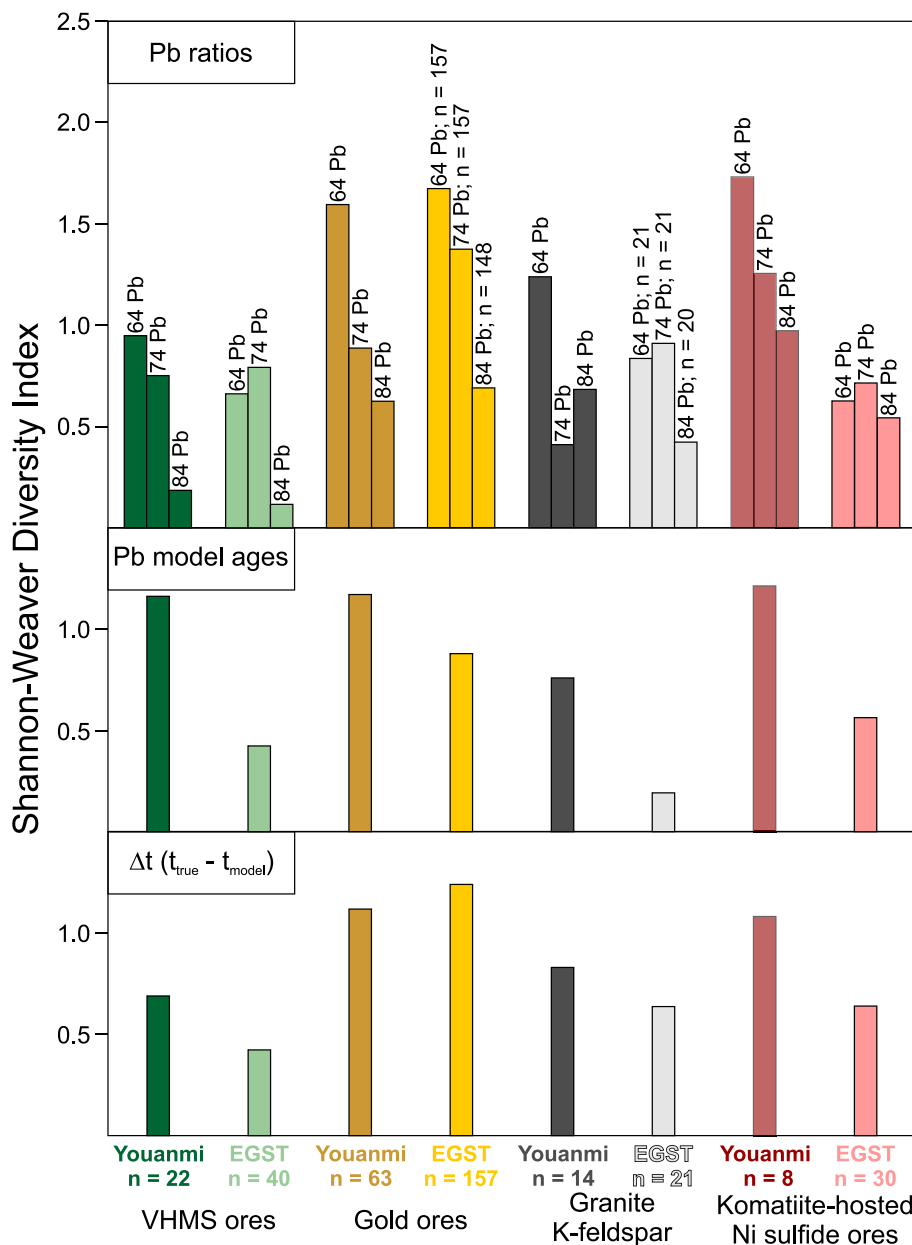
Fig. 6. Bar chart displaying Shannon-Weaver indices, which quantify the diversity of Pb isotope ratios and derivative parameters (Pb model ages, Δt) calculated for VHMS ore, gold ore, granite K-feldspar, and komatiite-hosted Ni sulfide ore samples in this study. The $^{206}Pb/^{204}Pb$ and $^{207}Pb/^{204}Pb$ ratios are more diverse than $^{208}Pb/^{204}Pb$ ratios in all chemical process groups with the minor exception of $^{207}Pb/^{204}Pb$ ratios in granite K-feldspar. Gold ores can be distinguished from the other groups, as their Shannon-Weaver indices are characterized by the greatest statistical diversity, most likely representing a larger Pb source variability. Komatiite-hosted Ni sulfide ores from the Youanmi Terrane (half-transparent red bars) show an elevated variability probably due to the small sample number. There is a general trend towards higher variability of Pb ratios and derivative parameters in the more crustal Youanmi Terrane, with again the exception of gold ores. Sample numbers of $^{206}Pb/^{204}Pb$, $^{207}Pb/^{204}Pb$, and $^{208}Pb/^{204}Pb$ ratios of gold ores and granite K-feldspar from the Eastern Goldfields Superterrane are not identical because of the lack of $^{208}Pb/^{204}Pb$ ratios for nine samples (gold ores) and one sample (granite K-feldspar), respectively, in the literature sources from which the Pb ratios were compiled. (For interpretation of the references to colour in this figure legend, the reader is referred to the web version of this article.)

(Figs. 9, 10, and 11; Zametzer et al., 2022); accordingly, the relative ^{206}Pb, ^{207}Pb, and ^{208}Pb deficit in EGST samples can be interpreted in the context of a stronger input of mantle Pb and/or younger crustal protolith ages (e.g., Milot et al., 2021; Hartnady et al., 2022; Zametzer et al., 2022). The statistically robust linear trend towards higher $^{207}Pb/^{204}Pb$ ratios through time (Fig. 11b) may underline the role of ^{207}Pb as a particularly sensitive indicator of crustal influence in granitic rocks from long-lived Archean terranes, either through contamination during granite emplacement or repetitive cycles of melting of preexisting mafic crust (e.g., Davis et al., 1996; Kamber et al., 2003, 2005; Halla, 2005, 2014, 2018b; Frost et al., 2006).

Archean granite Pb isotopic signatures can be variable, which enables investigation of the formation of the first continents and early crustal evolution (e.g., Oversby, 1975; Gariépy and Allègre, 1985; Hartnady et al., 2022). Nonetheless, the statistical diversity of Pb isotopic data from granite K-feldspar in the data set presented here is similar to that of VHMS ores and komatiite-hosted Ni sulfide ores from the EGST, but significantly lower than the variability of gold ores (Fig. 6). This observation is consistent with smaller variability in granite

source composition and age, probably due to a rather limited range of possible sources in Archean cratons which are dominated by TTG (tonalite-trondhjemite-granodiorite) assemblages (e.g., Barker and Arth, 1976; Champion and Sheraton, 1997; Martin, 1999; Champion and Smithies, 2007; Watkins et al., 2007; Laurent et al., 2014; Halla et al., 2017; Halla, 2018a; Moyen et al., 2018; Smithies et al., 2021). The implication of the difference in κ (that is seen in only one other process group; Table 2) is a subtle difference in the Th/U ratio between the Youanmi Terrane and the EGST. Even in strongly fractionated granites Th/U ratios have been shown to not change significantly in the continental crust (Wipperfurth et al., 2018), with the exception of S-type granites (e.g., Champion and Bultitude, 2013). Substantial κ variability would not be expected for the Yilgarn Craton where S-type granites have not been found (Witt and Davy, 1997a). The observed difference in our granite K-feldspar data can possibly be explained by a lack of sensitivity of the single-stage Pb evolution model used for the calculation of parameters to fully fingerprint source age variabilities. Early Pb isotopic work in the Yilgarn Craton (although confined to a relatively small region) recognized that granitic magmas must have experienced multi-
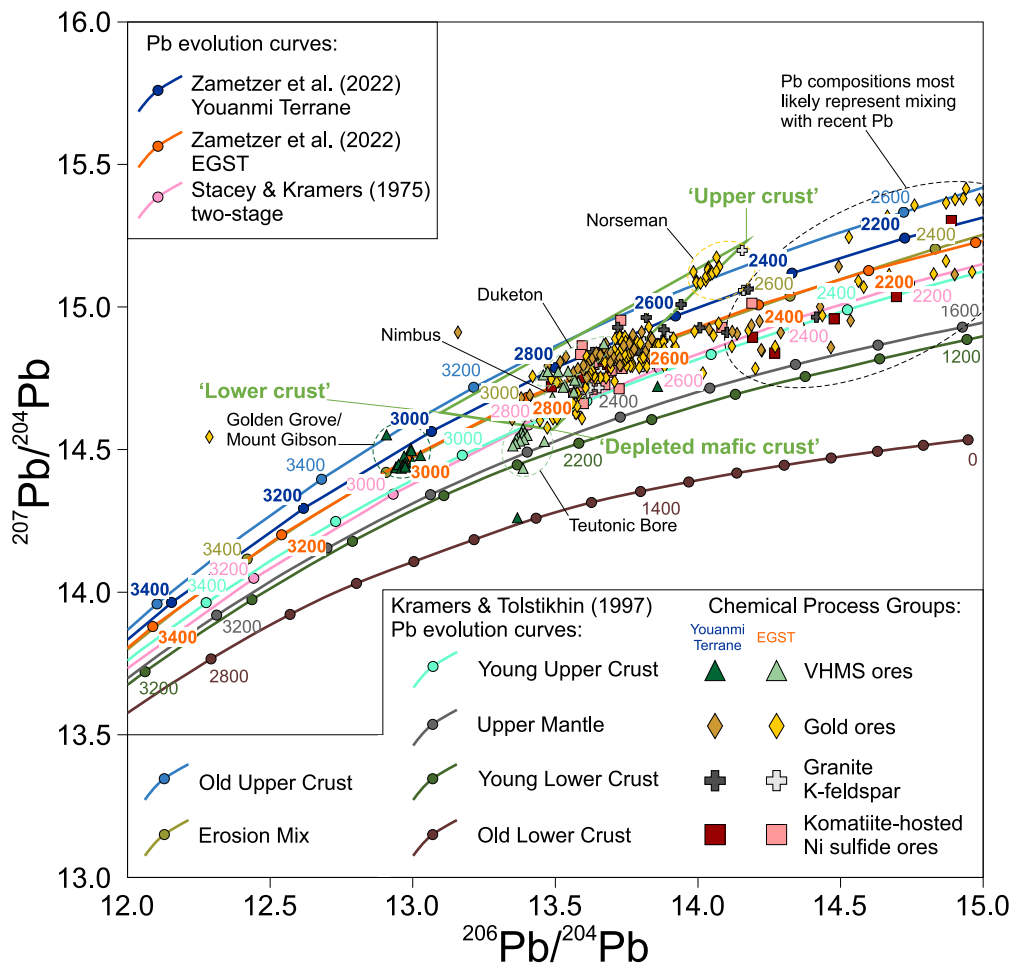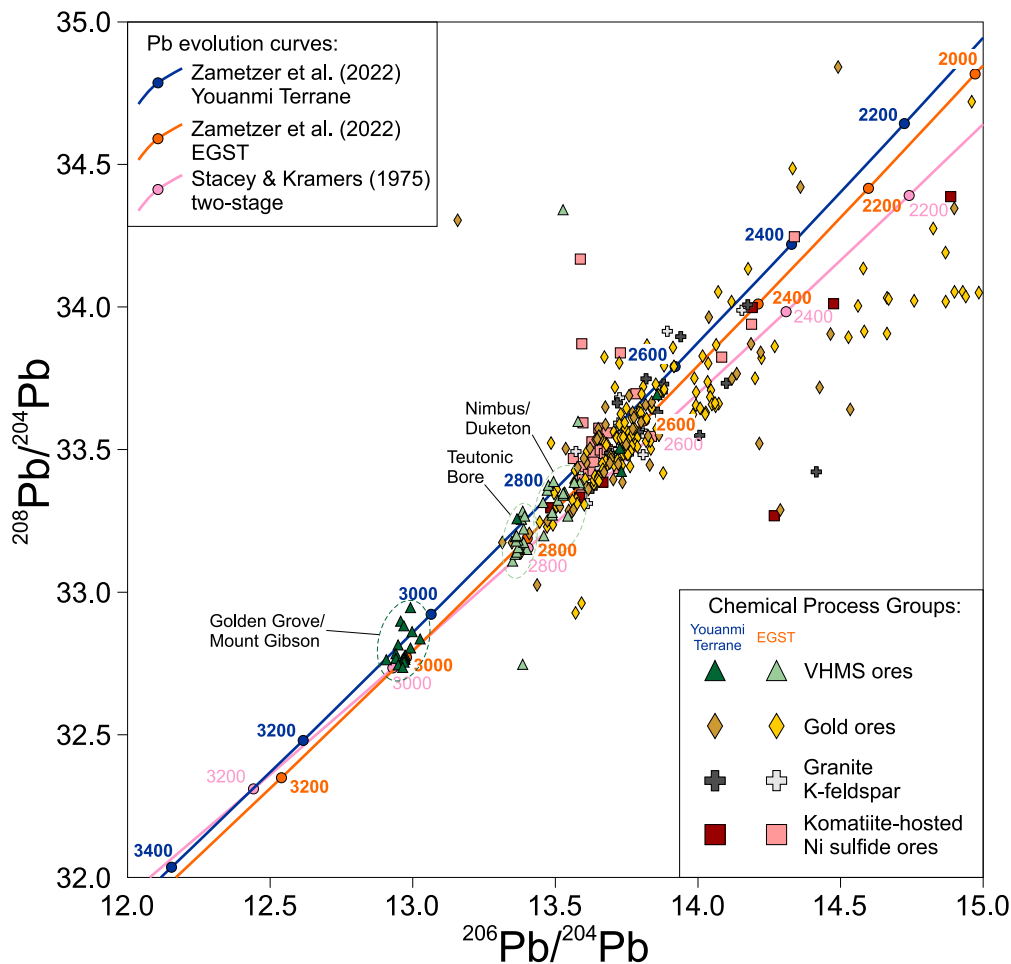
Fig. 7. Plot of all Pb isotopic data used in this contribution in $^{207}Pb/^{204}Pb$ vs. $^{206}Pb/^{204}Pb$ space. The blue and orange Pb growth curves are plotted using Pb evolution models for the Youanmi Terrane (blue) and the Eastern Goldfields Superterrane (orange) presented by Zametzer et al. (2022), which are based on the start date and initial Pb compositions of Maltese & Mezger's (2020) Pb evolution model for the Bulk Silicate Earth and calculated average Yilgarn Craton μ values. None of the multistage Pb growth curves for different crustal reservoirs after Kramers and Tolstikhin (1997) makes a good approximation of Pb evolution in the Yilgarn Craton. The green triangle is the compositional Pb source model for the Eastern Goldfields Superterrane after McNaughton and Groves (1996) with its three endmembers 'upper crust', 'depleted mafic crust', and 'lower crust'. A certain number of ore samples plots towards present-day (high $^{206}Pb/^{204}Pb$) compositions and most likely reflects mixed Pb signatures. Distinct sample groups are for instance high-μ gold ores from the Norseman area and low-μ VHMS ores from the Teutonic Bore camp in the Eastern Goldfields Superterrane. (For interpretation of the references to colour in this figure legend, the reader is referred to the web version of this article.)

stage Pb evolution histories prior to magma generation (Oversby, 1975, 1978).

Granitic magmas usually stem from mid to lower crustal melting (Barbarin, 1990) and may record processes associated with crustal contamination and fractionation of a formerly more juvenile melt (Fig. 2; e.g., Davis et al., 1996; Halla, 2005, 2014, 2018a, 2018b). The 'production' of granitic melts in the mid to lower crust is a direct result of large-scale differentiation (e.g., Haldar and Tišljar, 2014) owing to re-melting of protoliths (e.g., Watkins et al., 2007; Smithies et al., 2009; Laurent et al., 2013; Satkoski et al., 2013). Under Archean tectonic regimes, where horizontally directed processes were possibly less significant compared to present-day Earth (Bédard, 2018; Cawood et al., 2018), a prerequisite of the crystallization of large volumes of TTGs might have been accumulation and burial of hydrated mafic rocks (Kamber et al., 2005; Johnson et al., 2017; Mole et al., 2019). A significant thickness of mafic accumulations would have allowed slow cooling and stepwise differentiation of melts eventually resulting in granitic crust. However, geochemical and Hf isotopic evidence favors partial melting of basaltic rather than evolved precursors and not large-scale differentiation as the main driver of TTG or even granite formation (e.g., Satkoski et al., 2013; Huang et al., 2013b; Johnson et al., 2014), especially given that fractional crystallization from basaltic to granitic compositions may have been less prevalent in the Archean Eon (Kamber, 2015). Constant mantle-like oxygen isotope signatures in zircon that have been reported in a recent study for some TTG assemblages (Smithies et al., 2021) may be explained through re-melting of mantle-derived hydrated basalts and do not support 'stacked basalt' models of accumulation and burial. Yet more diverse O isotopic compositions in other TTGs might reflect melted basalts (Smithies et al., 2021). In

younger Archean terranes emplacement of TTGs is thought to have gradually waned while potassic granites (granite-monzogranite-syenogranite suites) began to crystallize contemporaneously (e.g., Taylor and McLennan, 1985; Frost et al., 2006; Smithies et al., 2009; Agangi et al., 2018; Halla, 2018a; Nebel et al., 2018; Moyen et al., 2021; André et al., 2022; Caton et al., 2022). The presence of K-feldspar in the granite samples investigated here is a general indicator of increased recycling of crust (Agangi et al., 2018), and/or crust-mantle interactions coinciding with the onset of plate tectonics (Laurent et al., 2014; Halla et al., 2017; Joshi et al., 2017; Halla, 2018a; Nebel et al., 2018) which are possible mechanisms leading to K-enrichment and diversification of granite compositions in the Neoarchean.

Based upon apparent negative correlations of μ and ω with granite whole rock geochemistry (Zametzer et al., 2022) and a trend to a stronger crustal Pb source influence with younger crystallization ages in Youanmi Terrane samples (Fig. 11), a possible additional signal in the K-feldspar Pb signatures is fractionation related to granite formation. The $^{206}Pb/^{204}Pb$ and $^{208}Pb/^{204}Pb$ ratios of granite K-feldspar samples plot closer to the reference linearization after Albarède and Juteau (1984) in comparison to VHMS ore samples (Figs. 9a and 10). In addition, granite K-feldspar has the highest median μ (8.86) of all sampling media and chemical process groups (Table 1) which reflects the less primitive nature of the granite K-feldspar samples. An enrichment with crustal Pb in younger granites, probably through progressive reworking, is seen in Youanmi Terrane samples (Fig. 11), while no such negative correlation between granite age and Pb ratios in EGST samples is best interpreted as a consequence of a greater mantle Pb source (Zametzer et al., 2022).

Fig. 8. Plot of all Pb isotopic data used in this contribution in $^{208}Pb/^{204}Pb$ vs. $^{206}Pb/^{204}Pb$ space. The blue and orange Pb growth curves are plotted using Pb evolution models for the Youanmi Terrane (blue) and the Eastern Goldfields Superterrane (orange) presented by Zametzer et al. (2022), which are based on the start date and initial Pb compositions of Maltese & Mezger's (2020) Pb evolution model for the Bulk Silicate Earth and calculated average Yilgarn Craton ω values. Data show a relatively systematic distribution with VHMS ore samples falling towards older Pb sources followed by komatiite-hosted Ni sulfide ores. Gold ores and granite K-feldspar samples predominantly indicate Pb sources between ~2700 and 2600 Ma. Distinct isolated sample groups are VHMS ores from the Golden Grove, Mount Gibson, and Teutonic Bore deposits. (For interpretation of the references to colour in this figure legend, the reader is referred to the web version of this article.)

6.3. Mineral deposit sources: the middle to upper crust

The presence of Pb in metal assemblages and fluid inclusions can be utilized to trace ore systems in the continental crust (Browning et al., 1987; Perring and McNaughton, 1992; Sanford, 1992; Tosdal et al., 1999; Huston et al., 2005, 2014, 2016; Champion and Huston, 2016; Tessalina et al., 2016; Bolhar et al., 2020). The origin of Pb in ore deposit systems may lie at deep crustal levels or even in the mantle (Groves, 1993; McNaughton and Groves, 1996; Qiu and McNaughton, 1999; Huston et al., 2014), depending on where the mineralized fluids were originally derived from. Leaching of the surrounding rocks at higher crustal levels through hydrothermal fluid flow may also deliver Pb (Doe and Stacey, 1974; Sanford, 1992). The range of median $\Delta\mu_{64}$-μ_{74} and Δt in Pb-rich ore minerals suggests that the quality of these sampling media (radiogenic ingrowth etc.) is not significantly different to granite K-feldspar (Tables 1 and 2). Data from different types of Pb-rich ore minerals reported here generally do not yield substantial differences between derivative parameters of the two most important minerals galena and pyrite (Tables 1 and 2). Median μ and ω are slightly lower than granite K-feldspar values, while k is very similar for all sampling media (Tables 1 and 2).
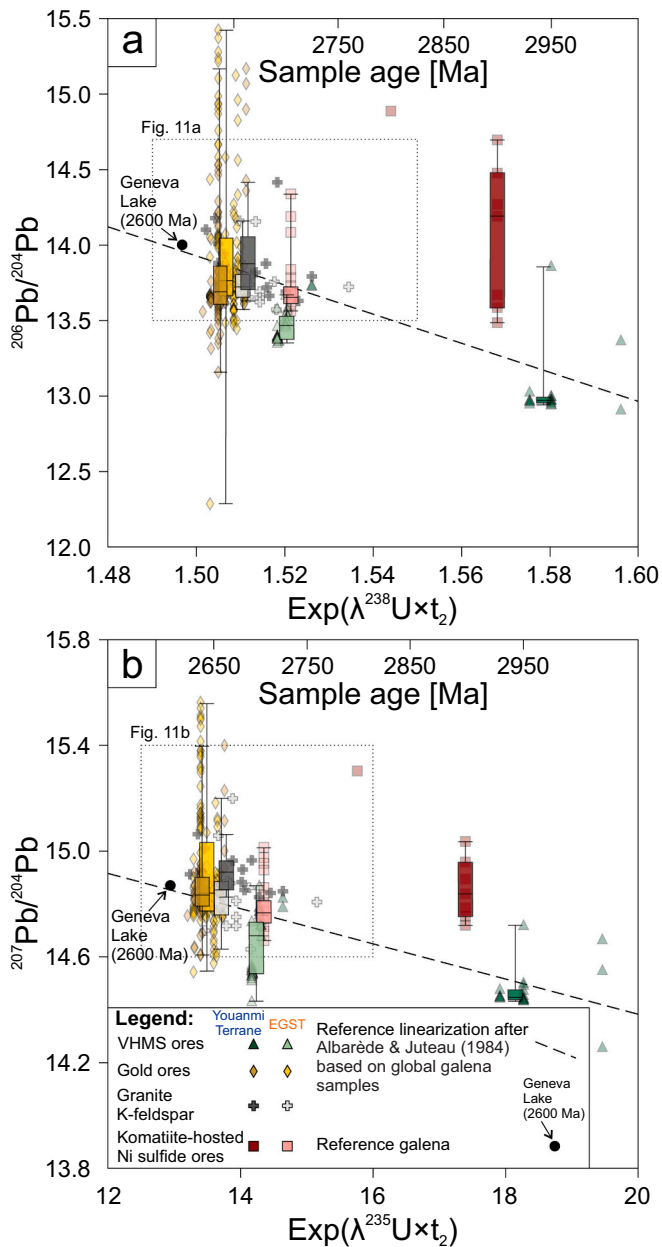
The interplay of processes that result in the development of VHMS, gold, and komatiite-hosted Ni sulfide deposits can be assigned to different crustal locations (Fig. 2) and, in the case of the Yilgarn Craton, to extensional (VHMS and komatiite-hosted Ni sulfides) and compressional (gold) geodynamic settings (e.g., Czarnota et al., 2010; Barnes et al., 2012; Huston et al., 2014; Mole et al., 2014; Hollis et al., 2015; Barrote et al., 2020a, 2020b).
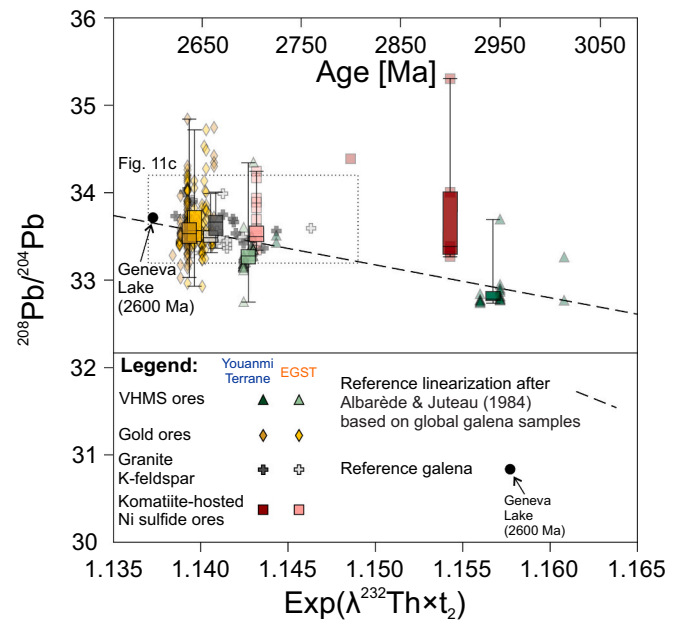
6.3.1. VHMS deposits

The mantle-derived Pb source signal in VHMS ore samples is possibly mixed with Pb sourced from felsic volcanic rocks and/or sediments (Fig. 2). Limited variability of Pb isotope ratios and derivative parameters in VHMS ores may indicate that Pb isotopic patterns can be utilized to distinguish between extensional geodynamic regimes (e.g., represented by VHMS or komatiite-hosted Ni sulfide deposits) and compressional or transpressional regimes (e.g., represented by orogenic gold deposits) on the terrane-scale. Dissimilarity in μ, ω, and Δt between different VHMS ore camps in uranogenic (Fig. 7) and thorogenic Pb space (Fig. 8) corresponds to pronounced variability in Archean μ values related to VHMS mineralization reported by Huston et al. (2010; see also Fig. 5 and Appendix A). This variability possibly reflects significant differences in crustal differentiation early in Earth's history that decreased with time through source reservoir mixing (Huston et al., 2010).

6.3.2. Gold deposits

Unlike VHMS deposits, most Yilgarn Craton gold deposits record peak mineralization events that are associated with high-grade ore enrichment during compressional (or transpressional) tectonic regimes (orogenic upgrades), while gold had been introduced earlier by felsic magmas (e.g., McDivitt et al., 2022). Thus, the deposits are commonly termed 'orogenic' (Groves, 1993; Groves et al., 1998; Goldfarb et al., 2001). Most of the gold deposits are epigenetic lode-gold deposits and structurally controlled products of a complex history of hydrothermal fluid flow channelized in shear zones, reverse faults, fractures, or along lithological boundaries in the mid to upper crust (Barnicoat et al., 1991; Groves, 1993; Groves et al., 1995, 1998; McNaughton and Groves, 1996;
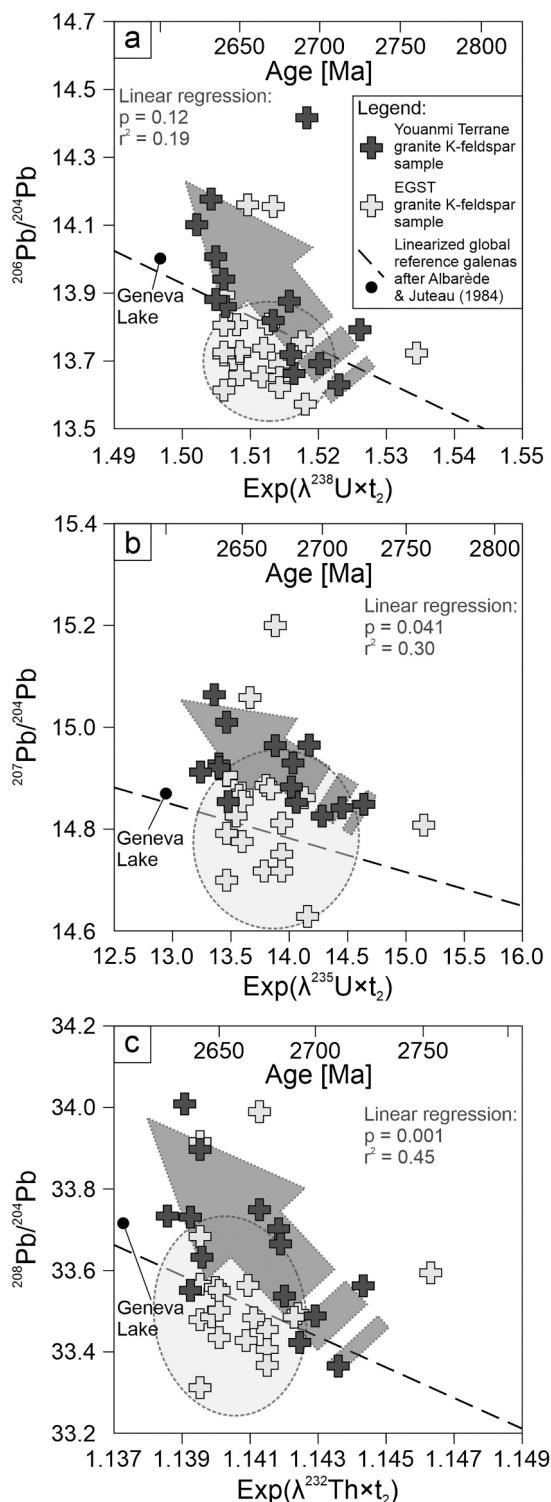
Fig. 10. Linearization of the Yilgarn Craton data set in inverted $^{208}Pb/^{204}Pb$ space after the format of Albarède and Juteau (1984). Box plots were calculated analogously to Fig. 9 and are displayed with median line, 75th and 25th percentiles, and maximum and minimum values, and laterally placed following the average age of the samples used in calculations. Data plot closely to the reference line in $^{208}Pb/^{204}Pb$ space. The VHMS ores have a deficit in ^{208}Pb relative to all other sampling media. Komatiite-hosted Ni sulfide ores samples from the Youanmi Terrane plot above the reference line and samples from the EGST close to the reference line.

Fig. 9. Linearization of the Yilgarn Craton data set after the format of Albarède and Juteau (1984). A reference line based on global galena samples is plotted in inverted $^{206}Pb/^{204}Pb$ (a) and $^{207}Pb/^{204}Pb$ (b) space. Box plots were calculated for the bulk of data points for each sampling medium, distinguishing between Youanmi Terrane and Eastern Goldfields Superterrane data sets and excluding samples that are separated from the bulk of data points by a crystallization/mineralization age (T) difference of 50 Ma or more. Box plots are displayed with median line, 75th and 25th percentiles, and maximum and minimum values, and laterally placed following the average age of the samples used in calculations. Decay constants $\lambda^{238}U$ and $\lambda^{235}U$ after Jaffey et al. (1971) and $\lambda^{232}Th$ after Steiger & Jaeger (1977) were used. Overall, the data set shows a tendency to a slight deficit in ^{206}Pb (a) and a weak enrichment in ^{207}Pb (b) relative to Albarède & Juteau's (1984) linearization. The VHMS ores have a deficit in ^{206}Pb (a) and ^{207}Pb (b) relative to all other sampling media. Komatiite-hosted Ni sulfide ores samples from the Youanmi Terrane plot above the reference line and samples from the EGST close to the reference line in both diagrams. Granite K-feldspar and gold ores generally have similar values, with lower $^{206}Pb/^{204}Pb$ and $^{207}Pb/^{204}Pb$ ratios in granite K-feldspar samples from the EGST relative to Youanmi Terrane samples. (For interpretation of the references to colour in this figure legend, the reader is referred to the web version of this article.)

Ridley et al., 1996; Witt and Vanderhor, 1998). This circulation of hydrothermal fluids modifies Pb isotopic signatures (Doe and Stacey, 1974; Perring and McNaughton, 1992; Wang et al., 1993; Qiu and McNaughton, 1999). Even though the majority of the large lode-gold deposits in the Yilgarn Craton formed or were upgraded during a very narrow time interval at ~2635 ± 10 Ma (Groves, 1993; Groves et al., 1995; Kent et al., 1996; Vielreicher et al., 2015), there is increasing structural (e.g., Bateman and Hagemann, 2004; Weinberg and van der Borgh, 2008; Blewett et al., 2010a; Bateman and Jones, 2015), geochronological and sulfur isotopic (Thébaud et al., 2018; Sugiono et al., 2021; McDivitt et al., 2022), and geochemical evidence (Smithies et al., 2018b) of polyphase gold mineralization related to magmatic intrusions that started in an earlier, extensional phase of deformation (see Appendix A for a compilation of the mineralization ages of all deposits dealt with in this work). The metamorphic grade of lode-gold deposits of the Yilgarn Craton spans sub-greenschist to granulite facies, with most between greenschist and lower amphibolite facies, which indicates a depth corresponding with mid to upper crustal levels (possibly comparable to granite production; Phillips et al., 1987; Barnicoat et al., 1991; Ridley et al., 1996). Some gold deposits (e.g., those around Wiluna) have epithermal textures that indicate an uppermost crustal level (Kent and Hagemann, 1996). The thickness of the crustal regime that was involved in the formation of the extensive gold deposits was determined to be greater than 15 km by Groves (1993). McNaughton and Groves (1996) reviewed and compiled EGST gold deposit-related Pb isotopic data and concluded that deeper crustal levels are likely to be the Pb source of the majority of EGST gold deposits. They documented a correspondence of Pb isotopic signatures in ores with signatures in EGST greenstones but not necessarily with Pb isotopic signatures in specific host rocks of individual deposits. Most samples from various media presented in our study are consistent with McNaughton and Groves' (1996) EGST Pb source model for gold deposits (Fig. 7).

The Pb isotope derivative parameters of gold ores do not record a

Fig. 11. Linearization of Yilgarn Craton granite K-feldspar samples after the format of Albarède and Juteau (1984). A reference line for comparison based on global galena samples is plotted in inverted $^{206}Pb/^{204}Pb$ (a), $^{207}Pb/^{204}Pb$ (b), and $^{208}Pb/^{204}Pb$ (c) space. A negative correlation between granite crystallization age and Pb ratios is visible in Youanmi Terrane samples (indicated by half-transparent dark grey arrows). As expressed by p and r^2 values referring to linear least squares regressions applied to the data, this relationship is statistically robust for $^{207}Pb/^{204}Pb$ and $^{208}Pb/^{204}Pb$ ratios, but not for $^{206}Pb/^{204}Pb$ ratios. EGST samples do not reflect such trend to a potentially more crustal nature of granite through time (indicated by half-transparent grey ellipsoids).

trend across the Ida Fault (Table 2; Figs. 5 and 6), which contrasts with the difference in Pb isotope ratios across this structure for all other chemical process groups. In addition, the larger diversity of Pb isotope ratios, calculated median Pb model ages, and Δt from Pb-rich gold ores allows discrimination from other process groups (Fig. 6). Gold ores have a very small $\Delta\mu_{64}$-μ_{74} (0.02; Table 1) which gives confidence in ascribing geological meaning to the dichotomy in Pb ratios and derivative parameters (Fig. 6). The heterogeneity likely documents a larger degree of Pb isotope variability in the source of the ore fluid. The wide variety of processes involved in the formation of gold deposits, and the structural control and variability in sources and source depth of hydrothermal fluids in particular, is interpreted to cause greater variation in the Pb isotopic signatures through Pb mixing. Possible Pb sources are rocks that had an originally mantle-derived Pb signature (e.g., primitive basalts), the extensive granites of the Yilgarn Craton and associated volcanic rocks, and upper crustal sediments (Qiu and McNaughton, 1999; Fig. 2).

Zones of unusually high μ values, e.g., identified by galenas of the Norseman gold deposits in the EGST presented by Perring and McNaughton (1990) can be explained in two ways: derivation from a source with more radiogenic compositions or an enrichment in Pb through assimilation with older crust along terrane boundaries and during accretionary processes. The Norseman gold deposits are located close to the Ida Fault (Fig. 1) – the older Youanmi Terrane crust was buried underneath the younger Kalgoorlie Terrane during compression and is likely to reflect a source of higher-μ Pb relative to Kalgoorlie Terrane material. This observation underpins early Pb isotopic work on acid-washed granite K-feldspar by Oversby (1975, 1978), as well as existing Nd and U-Pb zircon data (Compston et al., 1986; Campbell and Hill, 1988), and Hf isotopic data (Mole et al., 2014, 2019), all of which suggest an unusually old crustal block in the Norseman area.

6.3.3. Komatiite-hosted Ni sulfide deposits

Even though komatiite-hosted Ni sulfides sit in an extrusive rock, they are considered to reflect a significant proportion of mantle input (Herzberg, 1992; Barnes and Fiorentini, 2012; Mole et al., 2014; Sossi et al., 2016; Fig. 2). The rapid ascent of komatiitic melts during decompression melting of the mantle could render associated Ni sulfides a Pb source proxy for the upper mantle and/or the lower crust (Barnes and Fiorentini, 2012; Sossi et al., 2016). Plume tail-related volcanism and rifting along the eastern margin of the Youanmi Terrane and the western margin of the EGST has been proposed to have caused two major komatiite pulses at ~2900 and 2700 Ma (Hoatson et al., 2006; Barnes et al., 2012; Mole et al., 2014). Geochronological constraints broadly suggest formation of komatiite-hosted Ni sulfides in the Southern Cross Domain of the Youanmi Terrane at ~2900 Ma in the Forrestania greenstone belt (Perring et al., 1996; Mole et al., 2014) and at ~2800 Ma in the Lake Johnston Ni camp (Romano et al., 2013; Fig. 1; Appendix A). Mineralization of Ni sulfides in the Kambalda Region of the EGST can be related to the second komatiite emplacement event at ~2700 Ma and predates mineralization of komatiites in the southern Youanmi Terrane (Hoatson et al., 2006; Fiorentini, 2010; Mole et al., 2014; Fig. 1). A mantle signal could be preserved in the form of thorogenic Pb sources that appear to match the mineralization ages and on average are slightly older with respect to gold ores and granite K-feldspar in relation to Pb evolution models in $^{208}Pb/^{204}Pb$ vs. $^{206}Pb/^{204}Pb$ space (Fig. 8). The distinction between a higher-median-μ (10.19), -ω (44.05), and -Δt (625) Youanmi Terrane and a lower-median-μ (8.77), -ω (37.59), and -Δt (62) EGST is clearly visible in the Ni sulfide Pb ores (Table 2 and Fig. 5). High overall median values (μ > 10 and ω > 44 in the Youanmi Terrane) and the high $\Delta\mu_{64}$-μ_{74} of komatiite-hosted Ni sulfide ores from the Youanmi Terrane (1.76; Table 2) corroborate crustal contamination of the komatiites, which was also inferred by Perring et al. (1996) for komatiites of the southern Youanmi Terrane based upon geochemical analyses. Komatiite-associated Ni sulfide ores may indicate the general susceptibility of low-Pb mafic and ultramafic greenstone lithologies to modification (Lahaye et al., 1995) and

contamination of their Pb signature by pre-existing crust along their emplacement pathways. Komatiitic sulfides form when komatiites induce thermal erosion of substrate during extrusion, picking up crustal S (and presumably Pb), which then leads to sulfide saturation (Barnes and Fiorentini, 2012; compare also Bolhar et al., 2020). Sensitivity of greenstones from the Kambalda area to contamination with ancient crustal signatures was documented in a Pb isotopic study by Dupré and Arndt (1990). Yet komatiite-hosted Ni sulfide ore samples in our study record a significant difference in μ and ω across the Ida Fault (Fig. 5). The entire southern section of our case study area from the Forrestania Greenstone Belt in the Southern Cross Domain in the west to the Kambalda-Norseman region of the Kalgoorlie Terrane in the east appears to be a high-μ and high-ω zone, indicative of the previously inferred ancient crustal block at the margin of the Yilgarn Craton. This basement of protocrust could be relatively extensive with elevated μ and ω crossing the Ida Fault and most likely acting as one potential Pb source in this part of the Yilgarn Craton.

Several komatiite-hosted Ni sulfide ore samples plot towards younger Pb model ages (~2200–2400 Ma) in $^{207}Pb/^{204}Pb$ vs. $^{206}Pb/^{204}Pb$ space (Fig. 7) and may represent mixing through secondary hydrothermal fluids with more recent Pb signatures. The variability may also be caused by low Pb concentrations in the analyzed samples making them more prone to major changes in composition, e.g., due to minor later isotopic disturbance. The two least radiogenic samples yield Pb model ages of 2758 and 2701 Ma and μ (9.20, 9.35) and ω (39.87, 40.27) values that are high in the context of the entire sample set. Strong enrichment in ^{206}Pb, ^{207}Pb, and ^{208}Pb of komatiite-hosted Ni sulfide ore samples from the Youanmi Terrane (Figs. 9 and 10) hints at the sensitivity of this medium to Pb isotopic changes as well. The low number of Youanmi Terrane samples limits what can be definitively interpreted and likely explains why Shannon-Weaver diversity indices of these samples are closer to values from gold ores than to values from VHMS ores and komatiite-hosted Ni sulfide ores from the EGST (Fig. 6). Close alignment of the EGST samples to all three global galena reference lines (comparable to values from granite K-feldspar and gold ores) indicates that this data set is robust (Figs. 9 and 10) and isotopically less disturbed.

6.4. Inferences on crustal growth and evolution in the Yilgarn Craton

It is important to consider that μ, $\Delta\mu_{64}$-μ_{74}, ω, κ, Pb model ages, and Δt in this work have been calculated under the assumption of single-stage Pb evolution starting at 4498 Ma (Maltese and Mezger, 2020), which can only be an approximation to the real situation in the Yilgarn Craton with multiple mantle input events (Oversby, 1975, 1978; Mole et al., 2019; Zametzer et al., 2022). Nevertheless, the geochemical sensitivity of the single-stage model for the Yilgarn Craton appears sufficient to fingerprint differences in source U/Pb and Th/Pb between the Youanmi Terrane and the EGST (Zametzer et al., 2022). A generally good correspondence between Pb model ages and Δt with samples ages is observed (Tables 1 and 2 and Appendix A), supporting the predictive power of single-stage Pb evolution curves for the Yilgarn Craton.

The Neoarchean between ~2800 Ma and ~2500 Ma is considered a globally significant period of crustal development and cratonization (Condie and Alster, 2010; Hawkesworth et al., 2010, 2017; Kamber, 2015; Cawood et al., 2018). Our study area is one of the key geological archives documenting this period (Rowe et al., 2022). An average timing difference of source component extraction from the mantle in the Yilgarn Craton of ~200 Ma between an older and more crustal Youanmi Terrane and a younger and more juvenile EGST is seen in Nd and Hf isotopic data (e.g., Champion and Sheraton, 1997; Cassidy and Champion, 2004; Wyche et al., 2012; Champion, 2013; Mole et al., 2014, 2019; Lu et al., 2021a, 2021b). Differences in average μ, ω, and Δt (Table 2 and Fig. 5) and in the variability of Pb isotopic ratios, Pb model ages, and Δt (Fig. 6) between west and east of the Ida Fault follow this trend. Patterns analogous to the Nd and Hf isotopic systems are

documented in Pb data sets from granite K-feldspar, komatiite-hosted Ni sulfide ores, and VHMS ores (Figs. 5 and 6). This difference may reflect a change in either age, process, or bulk source U/Pb and Th/Pb composition related to the extraction of source components from the mantle. Calculations suggest that a timing difference between the initial crust-mantle fractionation events west and east of the Ida Fault is the main Pb isotopic signal (Appendix D). Nonetheless, an influence through changing bulk source composition on either side of the Ida Fault cannot be ruled out.

Low median μ and ω, old Pb model ages, the relative deficit in ^{206}Pb, and a slight deficit in ^{207}Pb and ^{208}Pb in VHMS ore samples (Figs. 9 and 10), as well as Pb isotopic variability between different VHMS camps (Fig. 6) point at this chemical process group as the most primitive (Tables 1 and 2). A secondary effect on Pb signatures is crustal contamination, as indicated by the very high μ, ω, and Δt values of komatiite-hosted Ni sulfide ores that are sensitive to Pb contamination due to low Pb concentrations. The correlation of granite K-feldspar μ and ω with granite geochemistry (e.g., Fe-number; Zametzer et al., 2022) and the statistically significant negative linear correlation of $^{207}Pb/^{204}Pb$ and $^{208}Pb/^{204}Pb$ ratios with granite age imply a relationship between the Pb signature and the degree of granite fractionation. This relationship is an indication of the sensitivity of the Pb isotope system to intracrustal processes such as the buildup of melts, fractionation, magma mixing and mingling, crustal contamination and recycling, hydrothermal fluid flow and fluid interaction, crystallization, mineralization, and radiogenic ingrowth in non-Pb-rich minerals and rocks. This sensitivity is further highlighted by the diverse Pb isotopic signatures in Pb-rich ores from gold deposits which have various mantle and crustal sources (Perring and McNaughton, 1992; Wang et al., 1993; McNaughton and Groves, 1996; Qiu and McNaughton, 1999). Widely sourced fluids may transport and potentially blur the Pb signature in gold ores. The population of ore samples that scatters towards younger Pb model compositions (higher $^{206}Pb/^{204}Pb$) in $^{207}Pb/^{204}Pb$ vs. $^{206}Pb/^{204}Pb$ (Fig. 7) and $^{208}Pb/^{204}Pb$ vs. $^{206}Pb/^{204}Pb$ space (Fig. 8) most likely represents the effects of recent hydrothermal fluids and blending with modern Pb compositions as well. Overall, the generally similar median μ, ω, κ, Pb model age, and Δt values (Table 1) – in particular in the EGST (Table 2) – indicate Pb isotopic assimilation in the continental crust. However, such isotopic mixing does not obliterate the large-scale timing (and/or bulk source composition) trend across the Ida Fault that remains visible in all process groups except gold ores.

Regional spatial patterns in Pb isotopic signatures are evident. For example, a zone between the Forrestania greenstone belt, Kambalda, and Norseman at the southern margin of the cration has higher source-μ and source-ω and areas with VHMS mineralization generally have lower μ and ω (e.g., Teutonic Bore), most likely reflecting significant extensional stages with mantle input.

A novel finding of this work is that the subtle difference between more crustal/more strongly recycled and more juvenile terranes is not only recorded in absolute values of Pb isotopic derivative parameters but also in the variability of Pb isotope ratios and respective parameters (Figs. 5 and 6). Values related to Youanmi Terrane samples are generally more heterogeneous than EGST values.

Vertically through the crust, a source-related signal, set by a specific U/Pb or Th/Pb ratio during crust-mantle fractionation is retained. Different lithologies from the crustal section express variable degrees of Pb signature modification due to crustal assimilation. Source differences (timing and potentially also composition) are interpreted as the primary signal in Pb isotopic data through various depths in the crust because of the spatial agreement with Nd and Hf trends. The commonality of the primary Pb isotopic signature across different crustal subsystems – as represented by different chemical process groups – suggests mass transport of U, Th, and Pb on the scale of the whole crustal column. Hence, a unified source of continental crust on either side of the Ida Fault is likely. The lithospheric sections of the Youanmi Terrane and the EGST evolved as entities and need not consist of allochthonous slices

(see also Mole et al., 2019).

7. Conclusions

Laser ablation Pb isotope protocols offer the advantage over dissolution-based approaches of relatively rapid analyses at the cost of analytical precision. Furthermore, time-resolved sampling and imaging of spot positions allows filtering to select signals best reflecting initial ratios.

The development of Earth's continental crust can be understood from a Pb isotope perspective by subdividing granite K-feldspar and ore Pb isotopic data into groups of geochemical proxies that link with the process at the Pb source. Yilgarn Craton Pb isotopic data from multiple process groups correlate with patterns in the whole rock Nd and zircon Hf isotope systems to suggest an isotopic boundary coincident with the crustal-scale Ida Fault. The difference in absolute μ, ω, and Δt values across the Ida Fault is documented in all process groups except Pb-rich ores from gold deposits. Moreover, an enhanced variability in Pb isotope ratios and derivative parameters is recorded in samples from the more crustal and more strongly recycled Youanmi Terrane in comparison with the more juvenile EGST, that shows more homogeneous Pb isotopic signatures. Horizontally, the distinction across the Ida Fault can be interpreted as reflecting a timing difference in the initial source fractionation event across the crust-mantle boundary.

The sensitivity of Pb isotopes to processes within the crust requires suitable means to unravel the resulting crustal assimilation. In addition to the examination of dichotomy between absolute values of Pb isotope derivative parameters, we suggest statistical analysis of Pb isotopic variability is useful for different chemical process groups for large Pb isotopic data sets that were collected over vast areas such as the Yilgarn Craton. Gold ores are influenced by a complex succession of processes causing mixing of fluids, and therefore of Pb from different sources, which may lead to diverse Pb isotopic signatures. The complexity of the processes involved, and consequently the Pb source variety, is recorded by the variability of Pb isotope ratios and derivative parameters and quantified by the Shannon-Weaver diversity index, at least allowing a distinction of gold deposit-related ore Pb data from other chemical process groups.

Different process groups have distinct signatures as a consequence of mixing ultimate source components. Corresponding patterns in different groups (e.g., across the Ida Fault) are interpreted to indicate a related initial Pb isotopic signal that is present in different geochemical sub-systems within the Yilgarn Craton's lithospheric section. Such commonality in isotopic signature implies mass transport of U, Th (and also Pb) from the crust-mantle boundary to upper crustal levels. Consequently, it is likely that blocks of continental crust in the Yilgarn Craton vertically evolved as entities and not separate units.

Declaration of Competing Interest

The authors declare that they have no known competing financial interests or personal relationships that could have appeared to influence the work reported in this paper.

Data availability

All research data are provided in the supplementary materials.

Acknowledgements

Appendix A. Supplementary data

Supplementary data to this article can be found online at https://doi.org/10.1016/j.chemgeo.2023.121327.

References

Agangi, A., Hofmann, A., Elburg, M.A., 2018. A review of Palaeoarchaean felsic volcanism in the eastern Kaapvaal craton: linking plutonic and volcanic records. Geosci. Front. 9, 667–688. https://doi.org/10.1016/j.gsf.2017.08.003.

Albarède, F., 1998. The growth of continental crust. Tectonophysics 296, 1–14. https://doi.org/10.1016/S0040-1951(98)00133-4.

Albarède, F., Juteau, M., 1984. Unscrambling the lead model ages. Geochim. Cosmochim. Acta 48, 207–212. https://doi.org/10.1016/0016-7037(84)90364-8.

Albarède, F., Desaulty, A.-M., Blichert-Toft, J., 2012. A geological perspective on the use of Pb isotopes in archaeometry. Archaeometry 54, 853–867. https://doi.org/10.1111/j.1475-4754.2011.00653.x.

Andersen, M.B., Stirling, C.H., Weyer, S., 2017. Uranium isotope fractionation. Rev. Mineral. Geochem. 82, 799–850. https://doi.org/10.2138/rmg.2017.82.19.

André, L., Monin, L., Hofmann, A., 2022. The origin of early continental crust: new clues from coupling Ge/Si ratios with silicon isotopes. Earth Planet. Sci. Lett. 582, 117415 https://doi.org/10.1016/j.epsl.2022.117415.

Appel, P.W.U., Moorbath, S., Taylor, P.N., 1978. Least radiogenic terrestrial lead from Isua, West Greenland. Nature 272, 524–526. https://doi.org/10.1038/272524a0.

Arcuri, G.A., Dickin, A.P., 2018. Pb Isotope Mapping of Paleoproterozoic Gneisses in the SW Grenville Province: evidence for a Cryptic Continental Suture. Geosciences 8, 247. https://doi.org/10.3390/geosciences8070247.

Armistead, S.E., Eglington, B.M., Pehrsson, S.J., 2021. PbIso: an R package and web app for calculating and plotting Pb isotope data. Earth ArXiv. https://doi.org/10.31223/X56G84.

Ayer, J.A., Dostal, J., 2000. Nd and Pb isotopes from the Lake of the Woods greenstone belt, northwestern Ontario: implications for mantle evolution and the formation of crust in the southern Superior Province. Can. J. Earth Sci. 37, 1677–1689. https://doi.org/10.1139/e00-067.

Barbarin, B., 1990. Granitoids: main petrogenetic classifications in relation to origin and tectonic setting. Geol. J. 25, 227–238. https://doi.org/10.1002/gj.3350250306.

Barker, F., Arth, J.G., 1976. Generation of trondhjemitic-tonalitic liquids and Archean bimodal trodhjemite-basalt suites. Geology 4, 596–600. https://doi.org/10.1130/0091-7613(1976)4<596:GOTLAA>2.0.CO;2.

Barnes, S.J., Fiorentini, M.L., 2012. Komatiite magmas and sulfide nickel deposits: a comparison of variably endowed Archean terranes. Econ. Geol. 107, 755–780. https://doi.org/10.2113/econgeo.107.5.755.

Barnes, S.J., Van Kranendonk, M.J., Sonntag, I., 2012. Geochemistry and tectonic setting of basalts from the Eastern Goldfields Superterrane. Aust. J. Earth Sci. 59, 707–735. https://doi.org/10.1080/08120099.2012.687398.

Barnicoat, A.C., Fare, R.J., Groves, D.I., McNaughton, N.J., 1991. Synmetamorphic lode-gold deposits in high-grade Archean settings. Geology 19, 921–924. https://doi.org/10.1130/0091-7613(1991)019<0921:SLGDIH>2.3.CO;2.

Barrote, V., Tessalina, S., McNaughton, N., Jourdan, F., Hollis, S.P., Ware, B., Zi, J.-W., 2020b. 4D history of the Nimbus VHMS ore deposit in the Yilgarn Craton, Western Australia. Precambrian Res. 337, 105536 https://doi.org/10.1016/j.precamres.2019.105536.

Barrote, V.R., McNaughton, N.J., Tessalina, S.G., Evans, N.J., Talavera, C., Zi, J.-W., McDonald, B.J., 2020a. The 4D evolution of the Teutonic Bore Camp VHMS deposits, Yilgarn Craton, Western Australia. Ore Geol. Rev. 120, 103448 https://doi.org/10.1016/j.oregeorev.2020.103448.

Bateman, R., Jones, S., 2015. Discussion: the timing of gold mineralization across the eastern Yilgarn Craton using U-Pb geochronology of hydrothermal phosphate minerals. Mineral. Deposita 50, 885–888. https://doi.org/10.1007/s00126-015-0609-9.

Bateman, R.J., Hagemann, S.G., 2004. Gold mineralisation throughout about 45 Ma of Archaean orogenesis: protracted flux of gold in the Golden Mile, Yilgarn Craton, Western Australia. Mineral. Deposita 39, 536–559. https://doi.org/10.1007/s00126-004-0431-2.

Bédard, J.H., 2018. Stagnant lids and mantle overturns: Implications for Archaean tectonics, magmagenesis, crustal growth, mantle evolution, and the start of plate tectonics. Geosci. Front. 9, 19–49. https://doi.org/10.1016/j.gsf.2017.01.005.

Blaxland, A.B., Aftalion, M., van Breemen, O., 1979. Pb isotopic composition of feldspars from Scottish Caledonian Granites, and the nature of the underlying crust. Scott. J. Geol. 15, 139–151. https://doi.org/10.1144/sjg15020139.

Blewett, R.S., Czarnota, K., Henson, P.A., 2010a. Structural-event framework for the eastern Yilgarn Craton, Western Australia, and its implications for orogenic gold. Precambrian Res. 183, 203–229. https://doi.org/10.1016/j.precamres.2010.04.004.

Blewett, R.S., Henson, P.A., Roy, I.G., Champion, D.C., Cassidy, K.F., 2010b. Scale-integrated architecture of a world-class gold mineral system: the Archaean eastern Yilgarn Craton, Western Australia. Precambrian Res. 183, 230–250. https://doi.org/10.1016/j.precamres.2010.06.004.

Blichert-Toft, J., Zanda, B., Ebel, D.S., Albarède, F., 2010. The Solar System primordial lead. Earth Planet. Sci. Lett. 300, 152–163. https://doi.org/10.1016/j.epsl.2010.10.001.

Bolhar, R., Kamber, B.S., Collerson, K.D., 2007. U–Th–Pb fractionation in Archaean lower continental crust: Implications for terrestrial Pb isotope systematics. Earth Planet. Sci. Lett. 254, 127–145. https://doi.org/10.1016/j.epsl.2006.11.032.

Bolhar, R., Hofmann, A., Kemp, A.I.S., Whitehouse, M.J., Wind, S., Kamber, B.S., 2017. Juvenile crust formation in the Zimbabwe Craton deduced from the O-Hf isotopic record of 3.8–3.1 Ga detrital zircons. Geochim. Cosmochim. Acta 215, 432–446. https://doi.org/10.1016/j.gca.2017.07.008.

Bolhar, R., Whitehouse, M.J., Milani, L., Magalhães, N., Golding, S.D., Bybee, G., LeBras, L., Bekker, A., 2020. Atmospheric S and lithospheric Pb in sulphides from the 2.06 Ga Phalaborwa phoscorite-carbonatite complex, South Africa. Earth Planet. Sci. Lett. 530, 115939 https://doi.org/10.1016/j.epsl.2019.115939.

Browning, P., Groves, D.I., Blockley, J.G., Rosman, K.J.R., 1987. Lead isotope constraints on the age and source of gold mineralization in the Archean Yilgarn Block, Western Australia. Econ. Geol. 82, 971–986. https://doi.org/10.2113/gsecongeo.82.4.971.

Calvert, A.J., Doublier, M.P., 2018. Archaean continental spreading inferred from seismic images of the Yilgarn Craton. Nat. Geosci. 11, 526–530. https://doi.org/10.1038/s41561-018-0138-0.

Campbell, I.H., Hill, R.I., 1988. A two-stage model for the formation of the granite-greenstone terrains of the Kalgoorlie-Norseman area, Western Australia. Earth Planet. Sci. Lett. 90, 11–25. https://doi.org/10.1016/0012-821X(88)90107-0.

Carignan, J., Gariépy, C., Machado, N., Rive, M., 1993. Pb isotopic geochemistry of granitoids and gneisses from the late Archean Pontiac and Abitibi Subprovinces of Canada. Chem. Geol. 106, 299–316. https://doi.org/10.1016/0009-2541(93)90033-F.

Carignan, J., Machado, N., Gariépy, C., 1995. Initial lead isotopic composition of silicate minerals from the Mulcahy layered intrusion: Implications for the nature of the Archean mantle and the evolution of greenstone belts in the Superior Province, Canada. Geochim. Cosmochim. Acta 59, 97–105. https://doi.org/10.1016/0016-7037(94)00375-V.

Carr, G.R., Dean, J.A., Suppel, D.W., Heithersay, P.S., 1995. Precise lead isotope fingerprinting of hydrothermal activity associated with Ordovician to Carboniferous metallogenic events in the Lachlan fold belt of New South Wales. Econ. Geol. 90, 1467–1505. https://doi.org/10.2113/gsecongeo.90.6.1467.

Cassidy, K.F., Champion, D.C., 2004. Crustal evolution of the Yilgarn Craton from Nd isotopes and granite geochronology: Implications for metallogeny. In: Muhling, J.R. (Ed.), SEG 2004, Predictive Mineral Discovery under Cover. Centre for Global Metallogeny, University of Western Australia, pp. 317–320.

Cassidy, K.F., Champion, D.C., McNaughton, N.J., Fletcher, I.R., Whitaker, A., Bastrakova, I.V., Budd, A.R., 2002. Characterisation and Metallogenic Significance of Archaean Granitoids of the Yilgarn Craton, Western Australia. MERIWA (Mineral and Energy Research Institute of Western Australia) Report No. 222.

Cassidy, K.F., Champion, D.C., Krapez, B., Barley, M.E., Brown, S.J.A., Blewett, R.S., Groenewald, P.B., Tyler, I.M., 2006. A revised geological framework for the Yilgarn Craton, Western Australia. Geol. Surv. West. Austra.Rec. 2006 (8), 1–8.

Castillo, P.R., MacIsaac, C., Perry, S., Veizer, J., 2018. Marine carbonates in the mantle source of oceanic basalts: Pb isotopic constraints. Sci. Rep. 8, 14932. https://doi.org/10.1038/s41598-018-33178-4.

Caton, S.A., Smit, M.A., Emo, R.B., Musiyachenko, K.A., Kielman-Schmitt, M., Kooijman, E., Scherstén, A., Halla, J., Bleeker, W., Hoffmann, J.E., Prakash Pandey, O., Ravindran, A., Maltese, A., Mezger, K., 2022. Evolution of the sources of TTG and associated rocks during the Archean from in-situ $^{87}Sr/^{86}Sr$ isotope analysis of apatite by LA-MC-ICPMS. Lithos 428-429, 106830. https://doi.org/10.1016/j.lithos.2022.106830.

Cawood, P.A., Hawkesworth, C.J., Pisarevsky, S.A., Dhuime, B., Capitanio, F.A., Nebel, O., 2018. Geological archive of the onset of plate tectonics. Philosop. Trans. Roy. Soc. A 376. https://doi.org/10.1098/rsta.2017.0405.

Champion, D.C., 2013. Neodymium depleted mantle model age map of Australia: explanatory notes and user guide. Record 2013/44. Geosci. Austra.: Canberra. https://doi.org/10.11636/Record.2013.044.

Champion, D.C., Bultitude, R.J., 2013. The geochemical and Sr-Nd isotopic characteristics of Paleozoic fractionated S-types granites of North Queensland: Implications for S-type granite petrogenesis. Lithos 162-163, 37–56. https://doi.org/10.1016/j.lithos.2012.11.022.

Champion, D.C., Huston, D.L., 2016. Radiogenic isotopes, ore deposits and metallogenic terranes: Novel approaches based on regional isotopic maps and the mineral systems concept. Ore Geol. Rev. 76, 229–256. https://doi.org/10.1016/j.oregeorev.2015.09.025.

Champion, D.C., Sheraton, J.W., 1997. Geochemistry and Nd isotope systematics of Archaean granites of the Eastern Goldfields, Yilgarn Craton, Australia: implications for crustal growth processes. Precambrian Res. 83, 109–132. https://doi.org/10.1016/S0301-9268(97)00007-7.

Champion, D.C., Smithies, R.H., 2007. Geochemistry of Paleoarchean granites of the East Pilbara Terrane, Pilbara Craton, Western Australia: implications for early Archean crustal growth. In: van Kranendonk, M.J., Smithies, R.H., Bennett, V.C. (Eds.), Earth's Oldest Rocks: Developments in Precambrian Geology, 15. Elsevier, pp. 369–409. https://doi.org/10.1016/S0166-2635(07)15043-X.

Chapman, N.D., Ferguson, M., Meffre, S.J., Stepanov, A., Maas, R., Ehrig, K.J., 2019. Pb isotopic constraints on the source of A-type Suites: Insights from the Hiltaba Suite – Gawler Range Volcanics Magmatic Event, Gawler Craton, South Australia. Lithos 346-347, 105156. https://doi.org/10.1016/j.lithos.2019.105156.

Chapman, N.D., Meffre, S.J., Mass, R., Ehrig, K., 2021. Pb-isotope ratios and the petrogenesis of the Tunkillia Suite, Gawler Craton. Aust. J. Earth Sci. 68, 1071–1091. https://doi.org/10.1080/08120099.2021.1915868.

Compston, W., Williams, I.S., Campbell, I.H., Gresham, J.J., 1986. Zircon xenocrysts from the Kambalda volcanics: age constraints and direct evidence for older continental crust below the Kambalda-Norseman greenstones. Earth Planet. Sci. Lett. 76, 299–311. https://doi.org/10.1016/0012-821X(86)90081-6.

Condie, K.C., 2000. Episodic continental growth models: Afterthoughts and extensions. Tectonophysics 322, 153–162. https://doi.org/10.1016/S0040-1951(00)00061-5.

Condie, K.C., Alster, R.C., 2010. Episodic zircon age spectra of orogenic granitoids: the supercontinent connection and continental growth. Precambrian Res. 180, 227–236. https://doi.org/10.1016/j.precamres.2010.03.008.

Condie, K.C., Kröner, A., 2013. The building blocks of continental crust: evidence for a major change in the tectonic setting of continental growth at the end of the Archean. Gondwana Res. 23, 394–402. https://doi.org/10.1016/j.gr.2011.09.011.

Cooper, C.M., Lenardic, A., Moresi, L., 2006. Effects of continental insulation and the partitioning of heat producing elements on the Earth's heat loss. Geophys. Res. Lett. 33, L13313. https://doi.org/10.1029/2006GL026291.

Cumming, G.L., Richards, J.R., 1975. Ore lead isotope ratios in a contiuously changing Earth. Earth Planet. Sci. Lett. 28, 155–171. https://doi.org/10.1016/0012-821X(75)90223-X.

Czarnota, K., Champion, D.C., Goscombe, B., Blewett, R.S., Cassidy, K.F., Henson, P.A., Groenewald, P.B., 2010. Geodynamics of the eastern Yilgarn Craton. Precambrian Res. 183, 175–202. https://doi.org/10.1016/j.precamres.2010.08.004.

Davis, W.J., Gariépy, C., van Breemen, O., 1996. Pb isotopic composition of late Archaean granites and the extent of recycling early Archaean crust in the Slave Province, Northwest Canada. Chem. Geol. 130, 255–269. https://doi.org/10.1016/0009-2541(96)00010-1.

Delavault, H., Dhuime, B., Hawkesworth, C., Marschall, H.R., 2018. Laser-ablation MC-ICP-MS lead isotope microanalysis down to 10 μm: application to K-feldspar inclusions within zircon. J. Anal. At. Spectrom. 33, 195–204. https://doi.org/10.1039/C7JA00276A.

DePaolo, D.J., 1988. Neodymium Isotope Geochemistry – An Introduction. Springer-Verlag, Berlin Heidelberg, p. 187.

DeWolf, C.P., Mezger, K., 1994. Lead isotope analyses of leached feldspars: constraints on the early crustal history of the Grenville Orogen. Geochim. Cosmochim. Acta 58, 5537–5550. https://doi.org/10.1016/0016-7037(94)90248-8.

Doe, B.R., 1967. The bearing of lead isotopes on the source of granitic magma. J. Petrol. 8, 51–83. https://doi.org/10.1093/petrology/8.1.51.

Doe, B.R., Stacey, J.S., 1974. The application of lead isotopes to the problems of ore genesis and ore prospect evaluation: a review. Econ. Geol. 69, 757–776. https://doi.org/10.2113/gsecongeo.69.6.757.

Doe, B.R., Zartman, R.E., 1979. Plumbotectonics, the Phanerozoic. In: Barnes, H.L. (Ed.), Geochemistry of Hydrothermal Ore Deposits, 2nd edition. John Wiley & Sons, New York, pp. 22–70.

Doucet, L.S., Li, Z.-X., Gamal El Dien, H., Pourteau, A., Murphy, J.B., Collins, W.J., Mattielli, N., Olierook, H.K.H., Spencer, C.J., Mitchell, R.N., 2020. Distinct formation history for deep-mantle domains reflected in geochemical differences. Nat. Geosci. 13, 511–515. https://doi.org/10.1038/s41561-020-0599-9.

Drummond, B.J., Goleby, B.R., Swager, C.P., 2000. Crustal signature of late Archaean tectonic episodes in the Yilgarn craton, Western Australia: evidence from deep seismic sounding. Tectonophysics 329, 193–221. https://doi.org/10.1016/S0040-1951(00)00196-7.

Dunphy, J.M., Fletcher, I.R., Cassidy, K.F., Champion, D.C., 2003. Compilation of SHRIMP U-Pb geochronological data, Yilgarn Craton, Western Australia, 2001-2002. Geosci. Austra. Rec. 2003/15, 139. http://pid.geoscience.gov.au/dataset/ga/41817.

Dupré, B., Arndt, N.T., 1990. Pb isotopic compositions of Archean komatiites and sulfides. Chem. Geol. 85, 35–56. https://doi.org/10.1016/0009-2541(90)90122-N.

Fiorentini, M.L., 2010. Chapter 4 – the Kambalda Nickel Camp. In: McCuaig, T.C., Miller, J.M., Beeresford, S. (Eds.), Controls on giant Mineral Systems in the Yilgarn Craton – A Field Guide. Geological Survey of Western Australia, Record, 2010/26, pp. 81–110.

Fletcher, I.R., Farquhar, R.M., 1982. The protocontinental nature and regional variability of the central metasedimentary belt of the Grenville Province: lead isotope evidence. Can. J. Earth Sci. 19, 239–253. https://doi.org/10.1139/e82-018.

Fletcher, I.R., McNaughton, N.J., 2001. Granitoid geochronology: SHRIMP zircon and titanite data. In: Champion, D.C., Cassidy, K.F. (Eds.), Characterisation and Metallogenic Significance of Archean Granitoids of the Yilgarn Craton, Western Australia (AMIRA Project P482/MERIWA Project M281). MERIWA Report 222, 6.1-6.158. Minerals and Energy Research Institute of Western Australia (MERIWA), Perth, WA, Australia. https://geodocs.dmirs.wa.gov.au/Web/documentlist/11/ReportNumber/222.

Fletcher, I.R., Dunphy, J.M., Cassidy, K.F., Champion, D.C., 2001. Compilation of SHRIMP U-Pb geochronological data, Yilgarn Craton, Western Australia, 2000-01. Geosci. Austra. Rec. 2001 (47), 110p. http://pid.geoscience.gov.au/dataset/ga/38156.

Franklin, J.M., Gibson, H.L., Jonasson, I.R., Galley, A.G., 2005. Volcanogenic Massive Sulfide Deposits. In: Hedenquist, J.W., Thompson, J.F.H., Goldfarb, R.J., Richards, J.

P. (Eds.), Economic Geology One Hundredth Anniversary Volume. The Economic Geology Publishing Company, pp. 523–560. https://doi.org/10.5382/AV100.17.

Frost, C.D., Frost, B.R., Kirkwood, R., Chamberlain, K.R., 2006. The tonalite-trondhjemite-granodiorite (TTG) to granodiorite-granite (GG) transition in the late Archean plutonic rocks of the Central Wyoming Province. Can. J. Earth Sci. 43, 1419–1444. https://doi.org/10.1139/e06-082.

Gancarz, A.J., Wasserburg, G.J., 1977. Initial Pb of the Amîtsoq gneiss, West Greenland, and implications for the age of the Earth. Geochim. Cosmochim. Acta 41, 1283–1301. https://doi.org/10.1016/0016-7037(77)90073-4.

Gardiner, N.J., Hickman, A.H., Kirkland, C.L., Lu, Y., Johnson, T., Zhao, J.-X., 2017. Processes of crust formation in the early Earth imaged through Hf isotopes from the East Pilbara Terrane. Precambrian Res. 297, 56–76. https://doi.org/10.1016/j.precamres.2017.05.004.

Gariépy, C., Allègre, C.J., 1985. The lead isotope geochemistry and geochronology of late-kinematic intrusives from the Abitibi greenstone belt, and the implications for late Archaean crustal evolution. Geochim. Cosmochim. Acta 49, 2371–2383. https://doi.org/10.1016/0016-7037(85)90237-6.

Gartmair, G., Barham, M., Kirkland, C.L., 2021. Detrital zircon perspectives on heavy mineral sands systems, Eucla Basin, Australia. Econ. Geol. https://doi.org/10.5382/econgeo.4871.

Gee, R.D., 1979. Structure and Tectonic style of the Western Australian Shield. Tectonophysics 58, 327–369. https://doi.org/10.1016/0040-1951(79)90315-9.

Goldfarb, R.J., Groves, D.I., Gardoll, S., 2001. Orogenic gold and geologic time: a global synthesis. Ore Geol. Rev. 18, 1–75. https://doi.org/10.1016/S0169-1368(01)00016-6.

Goldmann, A., Brennecka, G., Noordmann, J., Weyer, S., Wadhwa, M., 2015. The uranium isotopic composition of the earth and the solar system. Geochim. Cosmochim. Acta 148, 145–158. https://doi.org/10.1016/j.gca.2014.09.008.

Goleby, B.R., Blewett, R.S., Fomin, T., Fishwick, S., Reading, A.M., Henson, P.A., Kennett, B.L.N., Champion, D.C., Jones, L., Drummond, B.J., Nicoll, M., 2006. An integrated multi-scale 3D seismic model of the Archaean Yilgarn Craton, Australia. Tectonophysics 420, 75–90. https://doi.org/10.1016/j.tecto.2006.01.028.

Griffin, W.L., McGregor, V.R., Nutman, A., Taylor, P.N., Bridgwater, D., 1980. Early Archaean granulite-facies metamorphism south of Ameralik, West Greenland. Earth Planet. Sci. Lett. 50, 59–74. https://doi.org/10.1016/0012-821X(80)90120-3.

Groves, D.I., 1993. The crustal continuum model for late-Archaean lode-gold deposits of the Yilgarn Block, Western Australia. Mineral. Deposita 28, 366–374. https://doi.org/10.1007/BF02431596.

Groves, D.I., Ridley, J.R., Bloom, E.J.M., Gebre-Mariam, M., Hronsky, J.M.A., Knight, J.T., McNaughton, N.J., Ojala, V.J., Vielreicher, R.M., Holyland, P.W., McCuaig, T.C., 1995. Lode-gold deposits of the Yilgarn Block: Products of late-Archaean crustal-scale overpressured hydrothermal systems. In: Coward, M.P., Reis, A.C. (Eds.), Early Precambrian Processes. Geological Society of London Special Publication, vol. 95, pp. 155–172. https://doi.org/10.1144/GSL.SP.1995.095.01.10.

Groves, D.I., Goldfarb, R.J., Gebre-Mariam, M., Hagemann, S.G., Robert, F., 1998. Orogenic gold deposits: a proposed classification in the context of their crustal distribution and relationship to other gold deposit types. Ore Geol. Rev. 13, 7–27. https://doi.org/10.1016/S0169-1368(97)00012-7.

Gruau, G., Rosing, M., Bridgwater, D., Gill, R.C.O., 1996. Resetting of Sm-Nd systematics during metamorphism of > 3.7-Ga rocks: implications for isotopic models of early Earth differentiation. Chem. Geol. 133, 225–240. https://doi.org/10.1016/S0009-2541(96)00092-7.

Haldar, S.K., Tišljar, J., 2014. Introduction to Mineralogy and Petrology. Elsevier, p. 338. https://doi.org/10.1016/C2012-0-03337-6.

Halla, J., 2005. Late Archean high-Mg granitoids (sanukitoids) in the southern Karelian domain, eastern Finland: Pb and Nd isotopic constraints on crust-mantle interactions. Lithos 79, 161–178. https://doi.org/10.1016/j.lithos.2004.05.007.

Halla, J., 2014. Recycling of Lead at Neoarchean Continental margins. In: Dilek, Y., Furnes, H. (Eds.), Evolution of Archean Crust and Early Life. Modern Approaches in Solid Earth Sciences 7. Springer, Netherlands, Dordrecht, pp. 195–213. https://doi.org/10.1007/978-94-007-7615-9_8.

Halla, J., 2018a. Highlights on geochemical changes in Archaean granitoids and their implications for early Earth geodynamics. Geosciences 8, 353. https://doi.org/10.3390/geosciences8090353.

Halla, J., 2018b. Pb isotopes – a multi-function tool for assessing tectonothermal events and crust-mantle recycling at late Archaean convergent margins. Lithos 320-321, 207–221. https://doi.org/10.1016/j.lithos.2018.08.031.

Halla, J., Whitehouse, M.J., Ahmad, T., Bagai, Z., 2017. Archaean granitoids: An overview and significance from a tectonic perspective. In: Halla, J., Whitehouse, M.J., Ahmad, T., Bagai, Z. (Eds.), Crust-Mantle Interactions and Granitoid Diversification: Insights from Archaean Cratons, Geological Society of London Special Publications, vol. 449, pp. 1–18. https://doi.org/10.1144/SP449.10.

Hartnady, M.I.H., Kirkland, C.L., Smithies, R.H., Johnson, S.P., Johnson, T.E., 2022. Pb isotope insight into the formation of the Earth's first stable continents. Earth Planet. Sci. Lett. 578, 117319 https://doi.org/10.1016/j.epsl.2021.117319.

Hawkesworth, C.J., Kemp, A.I.S., 2006a. The differentiation and rates of generation of the continental crust. Chem. Geol. 226, 134–143. https://doi.org/10.1016/j.chemgeo.2005.09.017.

Hawkesworth, C.J., Kemp, A.I.S., 2006b. Using hafnium and oxygen isotopes in zircons to unravel the record of crustal evolution. Chem. Geol. 226, 144–162. https://doi.org/10.1016/j.chemgeo.2005.09.018.

Hawkesworth, C.J., Dhuime, B., Pietranik, A.B., Cawood, P.A., Kemp, A.I.S., Storey, C.D., 2010. The generation and evolution of the continental crust. J. Geol. Soc. 167, 229–248. https://doi.org/10.1144/0016-76492009-072.

Hawkesworth, C.J., Cawood, P.A., Dhuime, B., 2016. Tectonics and crustal evolution. GSA Today 26, 4–11. https://doi.org/10.1130/GSATG272A.1.

Hawkesworth, C.J., Cawood, P.A., Dhuime, B., Kemp, T.I.S., 2017. Earth's continental lithosphere through time. Annu. Rev. Earth Planet. Sci. 45, 169–198. https://doi.org/10.1146/annurev-earth-063016-020525.

Henry, P., Stevenson, R.K., Gariépy, C., 1998. Late Archean mantle composition and crustal growth in the Western Superior Province of Canada: neodymium and lead isotopic evidence from the Wawa, Quetico, and Wabigoon Subprovinces. Geochim. Cosmochim. Acta 62, 143–157. https://doi.org/10.1016/S0016-7037(97)00324-4.

Herzberg, C., 1992. Depth and degree of melting of komatiites. J. Geophys. Res. 97, 4521–4540. https://doi.org/10.1029/91JB03066.

Hiess, J., Condon, D.J., McLean, N., Noble, S.R., 2012. ^{238}U/^{235}U systematics in terrestrial uranium-bearing minerals. Science 335, 1610–1614. https://doi.org/10.1126/science.1215507.

Hoatson, D.M., Jaireth, S., Jaques, A.L., 2006. Nickel sulfide deposits in Australia: characteristics, resources, and potential. Ore Geol. Rev. 29, 177–241. https://doi.org/10.1016/j.oregeorev.2006.05.002.

Hofmann, A.W., 1988. Chemical differentiation of the Earth: the relationship between mantle, continental crust, and oceanic crust. Earth Planet. Sci. Lett. 90, 297–314. https://doi.org/10.1016/0012-821X(88)90132-X.

Hofmann, A.W., 1997. Mantle geochemistry: the message from oceanic volcanism. Nature 385, 219–229. https://doi.org/10.1038/385219a0.

Hollis, S.P., Yeats, C.J., Wyche, S., Barnes, S.J., Ivanic, T.J., Belford, S.M., Davidson, G.J., Roache, A.J., Wingate, M.T.D., 2015. A review of volcanic-hosted massive sulfide (VHMS) mineralization in the Archaean Yilgarn Craton, Western Australia: tectonic, stratigraphic and geochemical associations. Precambrian Res. 260, 113–135. https://doi.org/10.1016/j.precamres.2014.11.002.

Hollis, S.P., Yeats, C.J., Wyche, S., Barnes, S.J., Ivanic, T.J., 2017. VMS mineralization in the Yilgarn Craton, Western Australia: a review of known deposits and prospectivity analysis of felsic volcanic rocks. Geol. Surv. West. Austra. Report 165, 68p.

Hollocher, K., Ruiz, J., 1995. Major and trace element determinations on NIST glass standard reference materials 611, 612, 614 and 1834 by inductively coupled plasma-mass spectrometry. Geostand. Newslett. 19, 27–34. https://doi.org/10.1111/j.1751-908X.1995.tb00149.x.

Holmes, A., 1946. An estimate of the age of the earth. Nature 157, 680–684. https://doi.org/10.1038/157680a0.

Housh, T., Bowring, S.A., 1991. Lead isotopic heterogeneities within alkali feldspars: Implications for the determination of initial lead isotopic compositions. Geochim. Cosmochim. Acta 55, 2309–2316. https://doi.org/10.1016/0016-7037(91)90106-F.

Houtermans, F.G., 1946. Die Isotopenhäufigkeiten im natürlichen Blei und das Alter des Urans. Naturwissenschaften 33 (185–186), 219. https://doi.org/10.1007/BF00585229.

Huang, H., Polat, A., Fryer, B.J., 2013b. Origin of Archean tonalite-trondhjemite-granodiorite (TTG) suites and granites in the Fiskenæsset region, southern West Greenland: implications for continental growth. Gondwana Res. 23, 452–470. https://doi.org/10.1016/j.gr.2011.12.001.

Huang, Y., Chubakov, V., Mantovani, F., Rudnick, R.L., McDonough, W.F., 2013a. A reference Earth model for the heat-producing elements and associated geoneutrino flux. Geochem. Geophys. Geosyst. 14, 2003–2029. https://doi.org/10.1002/ggge.20129.

Huston, D.L., Champion, D.C., Cassidy, K.F., 2005. Tectonic controls on the endowment of Archean cratons in VHMS deposits: Evidence from Pb and Nd isotopes. In: Mao, J., Bierlein, F.P. (Eds.), Mineral Deposit Research: Meeting the Global Challenge. Springer, Berlin, Heidelberg, pp. 15–18. https://doi.org/10.1007/3-540-27946-6_4.

Huston, D.L., Pehrsson, S., Eglington, B.M., Zaw, K., 2010. The geology and metallogeny of volcanic-hosted massive sulfide deposits: variations through geologic time and with tectonic setting. Econ. Geol. 105, 571–591. https://doi.org/10.2113/gsecongeo.105.3.571.

Huston, D.L., Champion, D.C., Cassidy, K.F., 2014. Tectonic controls on the endowment of the Neoarchean Cratons in Volcanic-Hosted massive Sulfide deposits: evidence from Lead and Neodymium Isotopes. Econ. Geol. 109, 11–26. https://doi.org/10.2113/econgeo.109.1.11.

Huston, D.L., Champion, D.C., Mernagh, T.P., Downes, P.M., Jones, P., Carr, G., Forster, D., David, V., 2016. Metallogenesis and geodynamics of the Lachlan Orogen: new (and old) insights from spatial and temporal variations in lead isotopes. Ore Geol. Rev. 76, 257–267. https://doi.org/10.1016/j.oregeorev.2015.07.005.

Huston, D.L., Champion, D.C., Morrison, G., Maas, R., Thorne, J.P., Carr, G., Beams, S., Bottrill, R., Chang, Z.-S., Dhnaram, C., Downes, P.M., Forster, D.B., Gemmell, J.B., Lisitsin, V.A., McNeill, A., Vicary, M., 2017. Spatial variations in lead isotopes, Tasman Element, eastern Australia. Geosci. Austra. Rec. 2017 (09) https://doi.org/10.11636/Record.2017.009. Canberra.

Huston, D.L., Champion, D.C., Ware, B., Carr, G., Maas, R., Tessalina, S., 2019. Preliminary national-scale lead isotope maps of Australia. Geosci. Austra. Rec. 2019 (01) https://doi.org/10.11636/Record.2019.001.

Isnard, H., Gariépy, C., 2004. Sm-Nd, Lu-Hf, and Pb-Pb signatures of gneisses and granitoids from the La Grande belt: extent of late Archean crustal recycling in the northeastern Superior Province, Canada. Geochim. Cosmochim. Acta 68, 1099–1113. https://doi.org/10.1016/j.gca.2003.08.004.

Jaffey, A.H., Flynn, K.F., Glendenin, L.E., Bentley, W.C., Essling, A.M., 1971. Precision measurement of half-lives and specific activities of ^{235}U and ^{238}U. Phys. Rev. C 4, 1889–1906. https://doi.org/10.1103/PhysRevC.4.1889.

Johnson, T.E., Brown, M., Kaus, B.J.P., VanTongeren, J.A., 2014. Delamination and recycling of Archaean crust caused by gravitational instabilities. Nat. Geosci. 7, 47–52. https://doi.org/10.1038/ngeo2019.

Johnson, T.E., Brown, M., Gardiner, N.J., Kirkland, C.L., Smithies, R.H., 2017. Earth's first stable continents did not form by subduction. Nature 543, 239–242. https://doi.org/10.1038/nature21383.

Joshi, K.B., Bhattacharjee, J., Rai, G., Halla, J., Ahmad, T., Kurhila, M., Heilimo, E., Choudhary, A.K., 2017. The diversification of granitoids and plate tectonic implications at the Archaean-Proterozoic boundary in the Bundelkhand Craton, Central India. In: Halla, J., Whitehouse, M.J., Ahmad, T., Bagai, Z. (Eds.), Crust-Mantle Interactions and Granitoid Diversification: Insights from Archaean Cratons, Geological Society of London Special Publications, vol. 449, pp. 123–157. https://doi.org/10.1144/SP449.8.

Kamber, B.S., 2015. The evolving nature of terrestrial crust from the Hadean, through the Archaean, into the Proterozoic. Precambrian Res. 258, 48–82. https://doi.org/10.1016/j.precamres.2014.12.007.

Kamber, B.S., Collerson, K.D., 1999. Origin of ocean island basalts: a new model based on lead and helium isotope systematics. J. Geophys. Res. 104, 25479–25491. https://doi.org/10.1029/1999JB000258.

Kamber, B.S., Moorbath, S., 1998. Initial Pb of the Amîtsoq gneiss revisited: implication for the timing of early Archaean crustal evolution in West Greenland. Chem. Geol. 150, 19–41. https://doi.org/10.1016/S0009-2541(98)00059-X.

Kamber, B.S., Collerson, K.D., Moorbath, S., Whitehouse, M.J., 2003. Inheritance of early Archaean Pb-isotope variability from long-lived Hadean protocrust. Contrib. Mineral. Petrol. 145, 25–46. https://doi.org/10.1007/s00410-002-0429-7.

Kamber, B.S., Whitehouse, M.J., Bolhar, R., Moorbath, S., 2005. Volcanic resurfacing and the early terrestrial crust: Zircon U–Pb and REE constraints from the Isua Greenstone Belt, southern West Greenland. Earth Planet. Sci. Lett. 240, 276–290. https://doi.org/10.1016/j.epsl.2005.09.037.

Kanasewich, E.R., Farquhar, R.M., 1965. Lead isotope ratios from the Cobalt-Noranda Area, Canada. Can. J. Earth Sci. 2, 361–384. https://doi.org/10.1139/e65-029.

Kent, A.J.R., 2008. In-situ analysis of Pb isotope ratios using laser ablation MC-ICP-MS: controls on precision and accuracy and comparison between Faraday cup and ion counting systems. J. Anal. At. Spectrom. 23, 968–975. https://doi.org/10.1039/B801046C.

Kent, A.J.R., Hagemann, S.G., 1996. Constraints on the timing of lode-gold mineralisation in the Wiluna greenstone belt, Yilgarn Craton, Western Australia. Aust. J. Earth Sci. 43, 573–588. https://doi.org/10.1080/08120099608728278.

Kent, A.J.R., Cassidy, K.F., Fanning, C.M., 1996. Archean gold mineralization synchronous with the final stages of cratonization, Yilgarn Craton, Western Australia. Geology 24, 879–882. https://doi.org/10.1130/0091-7613(1996)024<0879:AGMSWT>2.3.CO;2.

Kinny, P.D., Maas, R., 2003. Lu–Hf and Sm–Nd isotope systems in zircon. Rev. Mineral. Geochem. 53, 327–341. https://doi.org/10.2113/0530327.

Korenaga, J., 2018. Crustal evolution and mantle dynamics through Earth history. Philos. Trans. R. Soc. A Math. Phys. Eng. Sci. 376 https://doi.org/10.1098/rsta.2017.0408, 20170408.

Kramers, J.D., Tolstikhin, I.N., 1997. Two terrestrial lead isotope paradoxes, forward transport modelling, core formation and the history of the continental crust. Chem. Geol. 139, 75–110. https://doi.org/10.1016/S0009-2541(97)00027-2.

Krishna Sinha, A., Tilton, G.R., 1973. Isotopic evolution of common lead. Geochim. Cosmochim. Acta 37, 1823–1849. https://doi.org/10.1016/0016-7037(73)90145-2.

Lahaye, Y., Arndt, N., Byerly, G., Chauvel, C., Fourcade, S., Gruau, G., 1995. The influence of alteration on the trace-element and Nd isotope compositions of komatiites. Chem. Geol. 126, 43–64. https://doi.org/10.1016/0009-2541(95)00102-1.

Laurent, O., Doucelance, R., Martin, H., Moyen, J.-F., 2013. Differentiation of the late-Archaean sanukitoid series and some implications for crustal growth: insights from geochemical modelling on the Bulai pluton, Central Limpopo Belt, South Africa. Precambrian Res. 227, 186–203. https://doi.org/10.1016/j.precamres.2012.07.004.

Laurent, O., Martin, H., Moyen, J.F., Doucelance, R., 2014. The diversity and evolution of late-Archean granitoids: evidence for the onset of "modern-style" plate tectonics between 3.0 and 2.5 Ga. Lithos 205, 208–235. https://doi.org/10.1016/j.lithos.2014.06.012.

Liebmann, J., Ware, B., Hartnady, M.I.H., Kirkland, C.L., 2022. Albany K-feldspar: A new Pb isotope reference material to unravel the evolution of old cratons. In: Conference Talk. Goldschmidt 2022, Honolulu, Hawaii.

Livermore, B.D., Connelly, J.N., Moynier, F., Bizzarro, M., 2018. Evaluating the robustness of a consens $^{238}U/^{235}U$ value for U-Pb geochronology. Geochim. Cosmochim. Acta 237, 171–183. https://doi.org/10.1016/j.gca.2018.08.014.

Lu, Y., Wingate, M.T.D., Kirkland, C.L., Hall, C.E., 2016. 182288: metagranodiorite, Horse Rocks. Geological survey of Western Australia Geochronology. Record 1350, 4.

Lu, Y., Wingate, M.T.D., Champion, D.C., Smithies, R.H., Johnson, S.P., Mole, D.R., Poujol, M., Zhao, J., Maas, R., Creaser, R.A., 2021a. Samarium-neodymium isotope map of Western Australia. Geol. Surv. West. Austra. Dig. Data Lay. https://www.dmirs.wa.gov.au/geoview.

Lu, Y., Wingate, M.T.D., Romano, S.S., Mole, D.R., Kirkland, C.L., Kemp, A.I.S., Belousova, E.A., Smithies, R.H., Gessner, K., Johnson, S.P., 2021b. Zircon lutetium-hafnium isotope map of Western Australia. Geol. Surv. West. Austra. Dig. Data Lay. www.dmirs.wa.gov.au/geoview.

Ludwig, K.R., Silver, L.T., 1977. Lead-isotope inhomogeneity in Precambrian igneous K-feldspars. Geochim. Cosmochim. Acta 41, 1457–1471. https://doi.org/10.1016/0016-7037(77)90251-4.

Maltese, A., Mezger, K., 2020. The Pb isotope evolution of Bulk Silicate Earth: Constraints from its accretion and early differentiation history. Geochim. Cosmochim. Acta 271, 179–193. https://doi.org/10.1016/j.gca.2019.12.021.

Martin, H., 1999. Adakitic magmas: modern analogues of Archaean granitoids. Lithos 46, 411–429. https://doi.org/10.1016/S0024-4937(98)00076-0.

McCuaig, T.C., Miller, J.M., Beeresford, S., 2010. Controls on giant mineral systems in the Yilgarn Craton - a field guide. Geol. Surv. West. Austr. Rec. 2010 (26), 164p.

McCulloch, M.T., Woodhead, J.D., 1993. Lead isotopic evidence for deep crustal-scale fluid transport during granite petrogenesis. Geochim. Cosmochim. Acta 57, 659–674. https://doi.org/10.1016/0016-7037(93)90376-8.

McDivitt, J.A., Hagemann, S.G., Kemp, A.I.S., Thébaud, N., Fisher, C.M., Rankenburg, K., 2022. U-Pb and Sm-Nd evidence for episodic orogenic gold mineralization in the Kalgoorlie gold camp, Yilgarn Craton, Western Australia. Econ. Geol. 117, 747–775. https://doi.org/10.5382/econgeo.4892.

McDonough, W.F., Sun, S.-S., 1995. The composition of the Earth. Chem. Geol. 120, 223–253. https://doi.org/10.1016/0009-2541(94)00140-4.

McNamara, G.S., Lesher, C.M., Kamber, B.S., 2017. New feldspar lead isotope and trace element evidence from the Sudbury Igneous complex indicate a complex origin of associated Ni-Cu-PGE mineralization involving underlying country rocks. Econ. Geol. 112, 569–590. https://doi.org/10.2113/econgeo.112.3.569.

McNaughton, N.J., Bickle, M.J., 1987. K-feldspar Pb-Pb isotope systematics of Archaean post-kinematic granitoid intrusions of the Diemals area, central Yilgarn Block, Western Australia. Chem. Geol. (Isotope Geosci. Sect.) 66, 193–208. https://doi.org/10.1016/0168-9622(87)90041-8.

McNaughton, N.J., Groves, D.I., 1996. A review of Pb-isotope constraints on the genesis of lode-gold deposits in the Yilgarn Craton, Western Australia. J. R. Soc. West. Aust. 79, 123–129.

Miller, J.S., Glazner, A.F., Farmer, G.L., Suayah, I.B., Keith, L.A., 2000. A Sr, Nd, and Pb isotopic study of mantle domains and crustal structure from Miocene volcanic rocks in the Mojave Desert, California. GSA Bull. 112, 1264–1279. https://doi.org/10.1130/0016-7606(2000)112<1264:ASNAPI>2.0.CO;2.

Milot, J., Blichert-Toft, J., Ayarzagüena Sanz, M., Fetter, N., Télouk, P., Albarède, F., 2021. The significance of galena Pb model ages and the formation of large Pb-Zn sedimentary deposits. Chem. Geol. 583, 120444 https://doi.org/10.1016/j.chemgeo.2021.120444.

Mole, D.R., Fiorentini, M.L., Thebaud, N., McCuaig, T.C., Cassidy, K.F., Kirkland, C.L., Wingate, M.T.D., Romano, S.S., Doublier, M.P., Belousova, E.A., 2012. Spatio-temporal constraints on lithospheric development in the southwest-central Yilgarn Craton, Western Australia. Aust. J. Earth Sci. 59, 625–656. https://doi.org/10.1080/08120099.2012.691213.

Mole, D.R., Fiorentini, M.L., Cassidy, K.F., Kirkland, C.L., Thebaud, N., McCuaig, T.C., Doublier, M.P., Duuring, P., Romano, S.S., Maas, R., Belousova, E.A., Barnes, S.J., Miller, J., 2013. Crustal evolution, intra-cratonic architecture and the metallogeny of an Archaean craton. In: Jenkin, G.R.T., Lusty, P.A.J., McDonald, I., Smith, M.P., Boyce, A.J., Wilkinson, J.J. (Eds.), Ore Deposits in an Evolving Earth, 393. Geological Society of London Special Publications, pp. 23–80. https://doi.org/10.1144/SP393.8.

Mole, D.R., Fiorentini, M.L., Thebaud, N., Cassidy, K.F., McCuaig, T.C., Kirkland, C.L., Romano, S.S., Doublier, M.P., Belousova, E.A., Barnes, S.J., Miller, J., 2014. Archean komatiite volcanism controlled by the evolution of early continents. Proc. Natl. Acad. Sci. U. S. A. 111, 100083–110088. https://doi.org/10.1073/pnas.1400273111.

Mole, D.R., Kirkland, C.L., Fiorentini, M.L., Barnes, S.J., Cassidy, K.F., Isaac, C., Belousova, E.A., Hartnady, M., Thebaud, N., 2019. Time-space evolution of an Archean craton: a Hf-isotope window into continent formation. Earth Sci. Rev. 196 https://doi.org/10.1016/j.earscirev.2019.04.003.

Moorbath, S., Welke, H., Gale, N.H., 1969. The significance of lead isotope studies in ancient, high-grade metamorphic basement complexes, as exemplified by the Lewisian rocks of Northwest Scotland. Earth Planet. Sci. Lett. 6, 245–256. https://doi.org/10.1016/0012-821X(69)90164-2.

Moorbath, S.M., Taylor, P.N., 1981. Isotopic evidence for continental growth in the Precambrian. In: Kroner, A. (Ed.), Precambrian Plate Tectonics. Developments in Precambrian Geology, vol. 4, pp. 491–525. https://doi.org/10.1016/S0166-2635(08)70025-2.

Moorbath, S.M., O'Nions, R.K., Pankhurst, R.J., 1975. The evolution of early Precambrian crustal rocks at Isua, West Greenland - geochemical and isotopic evidence. Earth Planet. Sci. Lett. 27, 229–239. https://doi.org/10.1016/0012-821X(75)90034-5.

Moyen, J.-F., Stevens, G., Kisters, A.F.M., Belcher, R.W., Lemirre, B., 2018. TTG plutons of the Barberton granitoid-greenstone terrain, South Africa. In: van Kranendonk, M., Bennett, V., Hoffmann, J.E. (Eds.), Earth's Oldest Rocks, 2nd edition. Elsevier, pp. 615–653. https://doi.org/10.1016/B978-0-444-63901-1.00025-3.

Moyen, J.-F., Zeh, A., Cuney, M., Dziggel, A., Carrouée, S., 2021. The multiple ways of recycling Archaean crust: a case study from the ca. 3.1 Ga granitoids from the Barberton Greenstone Belt, South Africa. Precambrian Res. 353, 105998 https://doi.org/10.1016/j.precamres.2020.105998.

Nebel, O., Capitanio, F.A., Moyen, J.-F., Weinberg, R.F., Clos, F., Nebel-Jacobsen, Y.J., Cawood, P.A., 2018. When crust comes of age: on the chemical evolution of Archaean, felsic continental crust by crustal drip tectonics. Philos. Trans. R. Soc. A Math. Phys. Eng. Sci. 376 https://doi.org/10.1098/rsta.2018.0103.

Nelson, D.R., 1997a. Compilation of SHRIMP U-Pb zircon geochronology data, 1996. Geol. Surv. West. Austr. Rec. 1997/2, 189.

Nelson, D.R., 1997b. Evolution of the Archaean granite-greenstone terranes of the Eastern Goldfields, Western Australia: SHRIMP U-Pb zircon constraints. Precambrian Res. 83, 57–81. https://doi.org/10.1016/S0301-9268(97)00005-3.

Nelson, D.R., 1998. Compilation of SHRIMP U-Pb zircon geochronology data, 1997. Geol. Surv. West. Austr. Rec. 1998 (2), 242.

Nelson, D.R., 1999. Compilation of geochronology data, 1998. Geol. Surv. West. Austr. Rec. 1999 (2), 222.

Osei, K.P., Kirkland, C.L., Mole, D.R., 2021. Nd and Hf isoscapes of the Yilgarn Craton, Western Australia and implications for its mineral systems. Gondwana Res. 92, 253–265. https://doi.org/10.1016/j.gr.2020.12.027.

Oversby, V.M., 1970. The isotopic composition of lead in iron meteorites. Geochim. Cosmochim. Acta 34, 65–75. https://doi.org/10.1016/0016-7037(70)90151-1.

Oversby, V.M., 1974. New look at the lead isotope growth curve. Nature 248, 132–133. https://doi.org/10.1038/248132a0.

Oversby, V.M., 1975. Lead isotopic systematics and ages of Archaean acid intrusives in the Kalgoorlie-Norseman area, Western Australia. Geochim. Cosmochim. Acta 39, 1107–1125. https://doi.org/10.1016/0016-7037(75)90053-8.

Oversby, V.M., 1976. Isotopic ages and geochemistry of Archaean acid igneous rocks from the Pilbara, Western Australia. Geochim. Cosmochim. Acta 40, 817–829. https://doi.org/10.1016/0016-7037(76)90034-X.

Oversby, V.M., 1978. Lead isotopes in Archaean Plutonic rocks. Earth Planet. Sci. Lett. 38, 237–248. https://doi.org/10.1016/0012-821X(78)90133-4.

Paton, C., Hellstrom, J., Paul, B., Woodhead, J., Hergt, J., 2011. Iolite: Freeware for the visualisation and processing of mass spectromic data. J. Anal. At. Spectrom. 26, 2508–2518. https://doi.org/10.1039/C1JA10172B.

Patterson, C., Tatsumoto, M., 1964. The significance of lead isotopes in detrital feldspar with respect to chemical differentiation within the Earth's mantle. Geochim. Cosmochim. Acta 28, 1–22. https://doi.org/10.1016/0016-7037(64)90052-3.

Paul, D., White, W.M., Turcotte, D.L., 2002. Modelling the isotopic evolution of the Earth. Philos. Trans. R. Soc. A Math. Phys. Eng. Sci. 360, 2433–2474. https://doi.org/10.1098/rsta.2002.1076.

Pawley, M.J., Wingate, M.T.D., Kirkland, C.L., Wyche, S., Hall, C.E., Romano, S.S., Doublier, M.P., 2012. Adding pieces to the puzzle: episodic crustal growth and a new terrane in the northeast Yilgarn Craton, Western Australia. Aust. J. Earth Sci. 59, 603–623. https://doi.org/10.1080/08120099.2012.696555.

Pearce, J.A., 2008. Geochemical fingerprinting of oceanic basalts with applications to ophiolite classification and the search for Archean oceanic crust. Lithos 100, 14–48. https://doi.org/10.1016/j.lithos.2007.06.016.

Pearce, N.J.G., Perkins, W.T., Westgate, J.A., Gorton, M.P., Jackson, S.E., Neal, C.R., Chenery, S.P., 1997. A compilation of new and published major and trace element data fo NIST SRM 610 and NIST SRM 612 glass reference materials. Geostand. Newslett. 21, 115–144. https://doi.org/10.1111/j.1751-908X.1997.tb00538.x.

Perring, C.S., McNaughton, N.J., 1990. Geological note: Proterozoic remobilization of ore metals within Archaean gold deposits: Lead isotope evidence from Norseman, Western Australia. Aust. J. Earth Sci. 37, 369–372. https://doi.org/10.1080/08120099008727934.

Perring, C.S., McNaughton, N.J., 1992. The relationship between Archaean gold mineralization and spatially associated minor intrusions at the Kambalda and Norseman gold camps, Western Australia: Lead isotope evidence. Mineral. Deposita 27, 10–22. https://doi.org/10.1007/BF00196076.

Perring, C.S., Barnes, S.J., Hill, R.E.T., 1996. Geochemistry of komatiites from Forrestania, Southern Cross Province, Western Australia: evidence for crustal contamination. Lithos 37, 181–197. https://doi.org/10.1016/0024-4937(95)00036-4.

Petrus, J.A., Kenny, G.G., Ayer, J.A., Lightfoot, P.C., Kamber, B.S., 2016. Uranium-lead zircon systematics in the Sudbury impact crater-fill: implications for target lithologies and crater evolution. J. Geol. Soc. 173, 59–75. https://doi.org/10.1144/jgs2014-056.

Pettke, T., Kodolányi, J., Kamber, B.S., 2018. From ocean to mantle: new evidence for U-cycling with implications for the HIMU source and the secular Pb isotope evolution of Earth's mantle. Lithos 316-317, 66–76. https://doi.org/10.1016/j.lithos.2018.07.010.

Phillips, G.N., Groves, D.I., Brown, I.J., 1987. Source requirements for the Golden Mile, Kalgoorlie: significance to the metamorphic replacement model for Archean gold deposits. Can. J. Earth Sci. 24, 1643–1651. https://doi.org/10.1139/e87-158.

Pidgeon, R.T., Wilde, S.A., 1990. The distribution of 3.0 Ga and 2.7 Ga volcanic episodes in the Yilgarn Craton of Western Australia. Precambrian Res. 48, 309–325. https://doi.org/10.1016/0301-9268(90)90015-I.

Piercey, S.J., 2011. The setting, style, and role of magmatism in the formation of volcanogenic massive sulfide deposits. Mineral. Deposita 46, 449–471. https://doi.org/10.1007/s00126-011-0341-z.

Qiu, Y.M., McNaughton, N.J., 1999. Source of Pb in orogenic lode-gold mineralisation: Pb isotope constraints from deep crustal rocks from the southwestern Yilgarn Craton, Australia. Mineral. Deposita 34, 366–381. https://doi.org/10.1007/s001260050210.

Qiu, Y.M., McNaughton, N.J., Groves, D.I., Dalstra, H.J., 1999. Ages of internal granitoids in the Southern Cross region, Yilgarn Craton, Western Australia, and their crustal evolution and tectonic implications. Aust. J. Earth Sci. 46, 971–981. https://doi.org/10.1046/j.1440-0952.1999.00758.x.

Quentin de Gromard, R., Ivanic, T.J., Zibra, I., 2021. Pre-Mesozoic interpreted bedrock geology of the southwest Yilgarn. Geol. Surv. West. Austra. Dig. Lay.

Ram Mohan, M., Piercey, S.J., Kamber, B.S., Srinivasa Sarma, D., 2013. Subduction related tectonic evolution of the Neoarchean eastern Dharwar Craton, southern India: New geochemical and isotopic constraints. Precambrian Res. 227, 204–226. https://doi.org/10.1016/j.precamres.2012.06.012.

Ridley, J., Mikucki, E.J., Groves, D.I., 1996. Archean lode-gold deposits: fluid flow and chemical evolution in vertically extensive hydrothermal systems. Ore Geol. Rev. 10, 279–293. https://doi.org/10.1016/0169-1368(95)00027-5.

Romano, S.S., Thébaud, N.J.M., Mole, D.R., Wingate, M.T.D., Kirkland, C.L., Doublier, M.P., 2013. Geochronological constraints on nickel metallogeny in the Lake Johnston belt, Southern Cross Domain. Aust. J. Earth Sci. 61, 143–157. https://doi.org/10.1080/08120099.2013.812579.

Rosholt, J.N., Zartman, R.E., Nkomo, I.T., 1973. Lead isotope systematics and uranium depletion in the granite mountains, Wyoming. Geol. Soc. Am. Bull. 84, 989–1002. https://doi.org/10.1130/0016-7606(1973)84<989:LISAUD>2.0.CO;2.

Rowe, M.L., Kemp, A.I.S., Wingate, M.T.D., Petersson, A., Whitehouse, M.J., van der Riet, C., 2022. Cratonisation of Archaean continental crust: Insights from U-Pb zircon geochronology and geochemistry of granitic rocks in the Narryer Terrane, northwest Yilgarn Craton. Precambrian Res. 372, 106609 https://doi.org/10.1016/j.precamres.2022.106609.

Sanford, R.F., 1992. Lead isotopic compositions and paleohydrology of caldera-related epithermal veins, Lake City, Colorado. Geol. Soc. Am. Bull. 104, 1236–1245. https://doi.org/10.1130/0016-7606(1992)104<1236:LICAPO>2.3.CO;2.

Satkoski, A.M., Bickford, M.E., Samson, S.D., Bauer, R.L., Mueller, P.A., Kamenov, G.D., 2013. Geochemical and Hf-Nd isotopic constraints on the crustal evolution of Archean rocks from the Minnesota River Valley, USA. Precambrian Res. 224, 36–50. https://doi.org/10.1016/j.precamres.2012.09.003.

Shannon, C.E., Weaver, W., 1949. The Mathematical Theory of Communication. University of Illinois Press, Urbana, p. 125.

Smithies, R.H., Champion, D.C., Van Kranendonk, M.J., 2009. Formation of Paleoarchean continental crust through infracrustal melting of enriched basalt. Earth Planet. Sci. Lett. 281, 298–306. https://doi.org/10.1016/j.epsl.2009.03.003.

Smithies, R.H., Ivanic, T.J., Lowrey, J.R., Morris, P.A., Barnes, S.J., Wyche, S., Lu, Y.-J., 2018a. Two distinct origins for Archean greenstone belts. Earth Planet. Sci. Lett. 487, 106–116. https://doi.org/10.1016/j.epsl.2018.01.034.

Smithies, R.H., Lu, Y., Kirkland, C.L., Cassidy, K.F., Champion, D.C., Sapkota, J., De Paoli, M., Burley, L., 2018b. A new look at lamprophyres and sanukitoids, and their relationship to the Black Flag Group and gold prospectivity. Geol. Surv. West. Austr. Rec. 2018 (15), 23.

Smithies, R.H., Lu, Y., Kirkland, C.L., Johnson, T.E., Mole, D.R., Champion, D.C., Martin, L., Jeon, H., Wingate, M.T.D., Johnson, S.P., 2021. Oxygen isotopes trace the origin of Earth's earliest continental crust. Nature 592, 70–75. https://doi.org/10.1038/s41586-021-03337-1.

Smosna, R., Bruner, K.B., Burns, A., 1999. Numerical analysis of sandstone composition, provenance, and paleogeography. J. Sediment. Res. 69, 1063–1070. https://doi.org/10.2110/jsr.69.1063.

Sossi, P.A., Eggins, S.M., Nesbitt, R.W., Nebel, O., Hergt, J.M., Campbell, I.H., O'Neill, H. St.C., van Kranendonk, M., Rhodri Davies, D., 2016. Petrogenesis and geochemistry of Archean komatiites. J. Petrol. 57, 147–184. https://doi.org/10.1093/petrology/egw004.

Spellerberg, I.F., Fedor, P.J., 2003. A tribute to Claude Shannon (1916-2001) and a plea for more rigorous use of species richness, species diversity and the 'Shannon-Wiener' Index. Glob. Ecol. Biogeogr. 12, 177–179. https://doi.org/10.1046/j.1466-822X.2003.00015.x.

Stacey, J.S., Kramers, J.D., 1975. Approximation of Terrestrial Lead Isotope Evolution by a Two-Stage Model. Earth Planet. Sci. Lett. 26, 207–221. https://doi.org/10.1016/0012-821X(75)90088-6.

Stacey, J.S., Delevaux, M.E., Ulrych, T.J., 1969. Some triple-filament lead isotope ratio measurements and an absolute growth curve for single-stage leads. Earth Planet. Sci. Lett. 6, 15–25. https://doi.org/10.1016/0012-821X(69)90154-X.

Stanton, R.L., Russell, R.D., 1959. Anomalous leads and the emplacement of lead sulfide ores. Econ. Geol. 54, 588–607. https://doi.org/10.2113/gsecongeo.54.4.588.

Steiger, R.H., Jäger, E., 1977. Subcommission on geochronology: convention on the use of decay constants in geo- and cosmochronology. Earth Planet. Sci. Lett. 36, 359–362. https://doi.org/10.1016/0012-821X(77)90060-7.

Stevenson, R., Henry, P., Gariépy, C., 1999. Assimilation-fractional crystallization origin of Archean sanukitoid suites: Western Superior Province, Canada. Precambrian Res. 96, 83–99. https://doi.org/10.1016/S0301-9268(99)00009-1.

Sugiono, D., Thébaud, N., LaFlamme, C., Fiorentini, M., Martin, L., Rogers, J., Lorusso, G., McFarlane, C., 2021. Integration of multiple sulfur isotopes with structural analysis unveils the evolution of ore fluids and source of sulfur at the Kanowna Belle Archean orogenic gold deposit, Yilgarn Craton, Western Australia. Mineral. Deposita. https://doi.org/10.1007/s00126-020-01032-1.

Sun, S.-S., Carr, G.R., Page, R.W., 1996. A continued effort to improve lead-isotope model ages. AGSO Res. Newslett. 24, 19–20.

Swager, C.P., Goleby, B.R., Drummond, B.J., Rattenbury, M.S., Williams, P.R., 1997. Crustal structure of granite-greenstone terranes in the Eastern Goldfields, Yilgarn Craton, as revealed by seismic reflection profiling. Precambrian Res. 83, 43–56. https://doi.org/10.1016/S0301-9268(97)00004-1.

Taylor, S.R., McLennan, S.M., 1985. The Continental Crust: Its Composition and Evolution. Blackwell Scientific Publications, p. 312.

Tessalina, S.G., Herrington, R.J., Taylor, R.N., Sundblad, K., Maslennikov, V.V., Orgeval, J.-J., 2016. Lead isotopic systematics of massive sulphide deposits in the Urals: applications for geodynamic setting and metal sources. Ore Geol. Rev. 72, 22–36. https://doi.org/10.1016/j.oregeorev.2015.06.016.

Thébaud, N., Sugiono, D., LaFlamme, C., Miller, J., Fisher, L., Voute, F., Tessalina, S., Sonntag, I., Fiorentini, M., 2018. Protracted and polyphased gold mineralisation in the Agnew District (Yilgarn Craton, Western Australia). Precambrian Res. 310, 291–304. https://doi.org/10.1016/j.precamres.2018.02.013.

Thorpe, R.I., 1999. The Pb isotope linear array for volcanogenic massive sulfide deposits of the Abitibi and Wawa Subprovinces, Canadian Shield. In: Hannington, M.D., Barrie, C.T. (Eds.), The Giant Kidd Creek volcanogenic massive sulfide deposit, Western Abitibi Subprovince, Canada, 10. Economic Geology Monograph, pp. 555–576. https://doi.org/10.5382/Mono.10.25.

Thorpe, R.I., Hickman, A.H., Davis, D.W., Mortensen, J.K., Trendall, A.F., 1992. Constraints to models for Archaean lead evolution from precise U-Pb geochronology for the Marble Bar region, Pilbara Craton, Western Australia. In: Glover, J.E., Ho, S. E. (Eds.), The Archaean: Terrains, Processes and Metallogeny, vol. 22. University of Western Australia, Geology Department (Key Centre) & University Extension, Publication, pp. 395–408.

Tosdal, R.M., Wooden, J.L., Bouse, R.M., 1999. Pb isotopes, ore deposits, and metallogenic terranes. In: Lambert, D.D., Ruiz, J. (Eds.), Application of Radiogenic Isotopes to Ore Deposit Research and Exploration. Reviews in Economic Geology, vol. 12, pp. 1–28. https://doi.org/10.5382/Rev.12.01.

Tyrrell, S., Haughton, P.D.W., Daly, J.S., Kokfelt, T.F., Gagnevin, D., 2006. The use of the common Pb isotope composition of detrital K-Feldspar grains as a provenance tool and its application to Upper Carboniferous paleodrainage, Northern England. J. Sediment. Res. 76, 324–345. https://doi.org/10.2110/jsr.2006.023.

Tyrrell, S., Haughton, P.D.W., Daly, J.S., Shannon, P.M., 2012. The Pb isotopic composition of detrital K-feldspar: A tool for constraining provenance, sedimentary processes and paleodrainage. In: Sylvester, P. (Ed.), Quantitative Mineralogy and Microanalysis of Sediments and Sedimentary Rocks. Mineralogical Association of Canada Short Course Series, vol. 42, pp. 203–217.

Van Kranendonk, M.J., Ivanic, T.J., Wingate, M.T.D., Kirkland, C.L., Wyche, S., 2013. Long-lived autochthonous development of the Archean Murchison Domain, and implications for Yilgarn Craton tectonics. Precambrian Res. 229, 49–92. https://doi.org/10.1016/j.precamres.2012.08.009.

Vervoort, J.D., White, W.M., Thorpe, R.I., 1994. Nd and Pb isotope ratios of the Abitibi greenstone belt: new evidence for very early differentiation of the Earth. Earth Planet. Sci. Lett. 128, 215–229. https://doi.org/10.1016/0012-821X(94)90146-5.

Vielreicher, N.M., Groves, D.I., McNaughton, N.J., Fletcher, I., 2015. The timing of gold mineralization across the eastern Yilgarn craton using U-Pb geochronology of hydrothermal phosphate minerals. Mineral. Deposita 50, 391–428. https://doi.org/10.1007/s00126-015-0589-9.

Wang, L.G., McNaughton, N.J., Groves, D.I., 1993. An overview of the relationship between granitoid intrusions and gold mineralisation in the Archaean Murchison Province, Western Australia. Mineral. Deposita 28, 482–494. https://doi.org/10.1007/BF02431604.

Wareham, C.D., Pankhurst, R.J., Thomas, R.J., Storey, B.C., Grantham, G.H., Jacobs, J., Eglington, B.M., 1998. Pb, Nd and Sr Isotope Mapping of Grenville-Age Crustal Provinces in Rodinia. J. Geol. 106, 647–660. https://doi.org/10.1086/516051.

Watkins, J.M., Clemens, J.D., Treloar, P.J., 2007. Archaean TTGs as sources of younger granitic magmas: melting of sodic metatonalites at 0.6-1.2 GPa. Contrib. Mineral. Petrol. 154, 91–110. https://doi.org/10.1007/s00410-007-0181-0.

Weinberg, R.F., van der Borgh, P., 2008. Extension and gold mineralization in the Archean Kalgoorlie Terrane, Yilgarn Craton. Precambrian Res. 161, 77–88. https://doi.org/10.1016/j.precamres.2007.06.013.

White, W.M., 1993. ^{238}U/^{204}Pb in MORB and open system evolution of the depleted mantle. Earth Planet. Sci. Lett. 115, 211–226. https://doi.org/10.1016/0012-821X(93)90223-V.

Wipperfurth, S.A., Guo, M., Šrámek, O., McDonough, W.F., 2018. Earth's chondritic Th/U: Negligible fractionation during accretion, core formation, and crust-mantle differentiation. Earth Planet. Sci. Lett. 498, 196–202. https://doi.org/10.1016/j.epsl.2018.06.029.

Witt, W.K., Davy, R., 1997a. Geology and geochemistry of Archaean granites in the Kalgoorlie region of the Eastern Goldfields, Western Australia: a syn-collisional tectonic setting? Precambrian Res. 83, 133–183. https://doi.org/10.1016/S0301-9268(97)00008-9.

Witt, W.K., Davy, R., 1997b. Geology and geochemistry of granitoid rocks in the southwest Eastern Goldfields Province. Geol. Surv. West. Austra. Report 49, 137.

Witt, W.K., Vanderhor, F., 1998. Diversity within a unified model for Archaean gold mineralization in the Yilgarn Craton of Western Australia: an overview of the late-orogenic, structurally-controlled gold deposits. Ore Geol. Rev. 13, 29–64. https://doi.org/10.1016/S0169-1368(97)00013-9.

Wooden, J.L., Mueller, P.A., 1988. Pb, Sr, and Nd isotopic compositions of a suite of late Archean, igneous rocks, eastern Beartooth Mountains: implications for crust-mantle evolution. Earth Planet. Sci. Lett. 87, 59–72. https://doi.org/10.1016/0012-821X(88)90064-7.

Woodhead, J.D., Hergt, J.M., 2001. Strontium, neodymium and lead isotope analyses of NIST glass certified reference materials: SRM 610, 612, 614. Geostand. Newslett. 25, 261–266. https://doi.org/10.1111/j.1751-908X.2001.tb00601.x.

Wyche, N.L., Wyche, S., 2017. Yilgarn Craton Geology. In: Phillips, G.N. (Ed.), Australian Ore Deposits. The Australasian Institute of Mining and Metallurgy, Melbourne, Monograph, vol. 32, pp. 89–94.

Wyche, S., Kirkland, C.L., Riganti, A., Pawley, M.J., Belousova, E., Wingate, M.T.D., 2012. Isotopic constraints on stratigraphy in the central and eastern Yilgarn Craton, Western Australia. Aust. J. Earth Sci. 59, 657–670. https://doi.org/10.1080/08120099.2012.697677.

Wyche, S., Ivanic, T.J., Zibra, I., 2013. Youanmi and Southern Carnarvon seismic and magnetotelluric (MT) workshop 2013. Geol. Surv. West. Austr. Rec. 2013 (6), 180p.

Wyche, S., Lu, Y., Wingate, M.T.D., 2019. In: Van Kranendonk, M.J., Bennett, V.C., Hoffmann, J.E. (Eds.), Evidence of Hadean to Paleoarchean Crust in the Youanmi and South West Terranes, and Eastern Goldfields Superterrane of the Yilgarn Craton, Western Australia, Second edition. Earth's Oldest Rocks, pp. 279–292. https://doi.org/10.1016/B978-0-444-63901-1.00013-7.

Yeats, C.J., McNaughton, N.J., Groves, D.I., 1996. SHRIMP U-Pb geochronological constraints on Archean volcanic-hosted massive sulfide and lode gold mineralization at Mount Gibson, Yilgarn Craton, Western Australia. Econ. Geol. 91, 1354–1371. https://doi.org/10.2113/gsecongeo.91.8.1354.

Zametzer, A., Kirkland, C.L., Hartnady, M.I.H., Barham, M., Champion, D.C., Bodorkos, S., Smithies, R.H., Johnson, S.P., 2022. Applications of Pb isotopes in granite K-feldspar and Pb evolution in the Yilgarn Craton. Geochim. Cosmochim. Acta 320, 279–303. https://doi.org/10.1016/j.gca.2021.11.029.

Zartman, R.E., Doe, B.R., 1981. Plumbotectonics-the model. Tectonophysics 75, 135–162. https://doi.org/10.1016/0040-1951(81)90213-4.

Zartman, R.E., Haines, S.M., 1988. The plumbotectonic model for Pb isotopic systematics among major terrestrial reservoirs – a case for bi-directional transport. Geochim. Cosmochim. Acta 52, 1327–1339. https://doi.org/10.1016/0016-7037(88)90204-9.

Zartman, R.E., Wasserburg, G.J., 1969. The isotopic composition of lead in potassium feldspars from some 1.0-b.y. old north American igneous rocks. Geochim. Cosmochim. Acta 33, 901–942. https://doi.org/10.1016/0016-7037(69)90104-5.

Zen, E., 1986. Aluminum enrichment in silicate melts by fractional crystallization: some mineralogic and petrographic constraints. J. Petrol. 27, 1095–1117. https://doi.org/10.1093/petrology/27.5.1095.